Topology of hydrothermal waves in liquid bridges and dissipative structures of transported particles

Roman V. Mukin* and Hendrik C. Kuhlmann†

Institute of Fluid Mechanics and Heat Transfer, Vienna University of Technology, Resselgasse 3, 1040 Vienna, Austria

(Received 14 August 2013; published 21 November 2013)

High-resolution three-dimensional numerical simulations are carried out for hydrothermal waves in a thermocapillary liquid bridge with Prandtl number $\mathrm{Pr} = 4$ and length-to-radius aspect ratio $\Gamma = 0.66$. The flow topology is analyzed using Poincaré sections in a frame of reference co-rotating with the phase velocity of the wave. We find regions of regular and chaotic motion. The regular regions are shown to be of key importance for dissipative structures of transported particles. Suspended particles which are passively advected in the bulk, but experience dissipation in a thin layer below the free surface, can rapidly form dissipative structures, also called particle accumulation structures. The shape and the formation time of the particulate structures are determined by the location of the invariant tori of the flow field with respect to the sub-surface layer in which the dissipation of the particle motion acts. The results from a hard-wall particle–free-surface interaction model are in good agreement with experimental observations.

DOI: 10.1103/PhysRevE.88.053016 PACS number(s): 47.52.+j, 47.55.nb, 47.54.−r, 45.70.Qj

I. INTRODUCTION

Thermocapillary flows play an important role in nature and in many technical applications like, e.g., crystal growth [1] or laser welding [2]. Motivated by the floating-zone crystal-growth technique the half-zone model has been developed, aimed at understanding the origin of crystal striations [3]. The half-zone model consists of a liquid drop supported by surface tension between two coaxial cylindrical rods. When the supporting rods are heated differentially a flow is driven in the liquid via the thermocapillary effect. The half-zone model was very successful in relating the crystal striations to the onset of flow oscillations which cause time-dependent condition at the crystal-melt interface. The model is probably the most extensively studied thermocapillary-flow system and it has emerged as a paradigm for thermocapillary flows [4–7].

The half-zone problem, also called the thermocapillary liquid bridge, has recently attracted a renewed interest since the discovery by Schwabe *et al.* [8] that small particles suspended in a high-Prandtl-number liquid bridge can rapidly form regularly ordered structures from an initially unordered particle-configuration state. These structures are called particle-accumulation structures (PAS). Particle-accumulation structures have only been observed when the flow is an azimuthally *traveling* hydrothermal wave but not when the flow is an azimuthally *standing* wave. Most attention has been paid to those particle-accumulation patterns in which the particles align themselves into distinct closed threads which can take different shapes. All threads observed to date rotate, like solid bodies, about the axis of the half zone with the same angular velocity as the hydrothermal wave. It is important to note that only the pattern rotates but not the individual particles. Therefore, PAS differs from the trajectory of any individual particle trajectory in the laboratory frame of reference.

The phenomenon was experimentally investigated by Tanaka *et al.* [9], Schwabe *et al.* [10,11], and Abe *et al.* [12]. By visual observation Schwabe *et al.* [11] estimated the dependence of the formation time of PAS after both the particle pattern and the hydrothermal wave have been destructed by intentional mechanical perturbations (stirring the liquid). From the measurements of the combined traveling wave and PAS formation time [11] it can be concluded that the particles must have a certain minimum size to be able to form PAS. Moreover, PAS are formed most rapidly if the particle density matches the density of the liquid. The latter observation strongly suggests that Stokes drag is not the primary reason for the particle accumulation, at least not in the bulk of the liquid bridge where the velocity field is smooth. This is consistent with the observation that PAS are also formed under zero-gravity conditions [10], an observation which excludes buoyancy as a mechanism for PAS formation.

Hofmann and Kuhlmann [13] have suggested that the accumulation is due to the interaction of finite-size particles with the free surface. In fact, most particles must pass by the free surface in a very close distance as the highest flow velocities arise at or near the free surface. By treating the particles as perfect tracers in the bulk and assuming that the particles cannot cross a cylindrical surface $R^* < R$, where R is the radius of the liquid bridge Hofmann and Kuhlmann [13] found that particles can become rapidly attracted to a trajectory which is closed in the coordinate system corotating with the hydrothermal wave. They found that the closed particle trajectory is identical with a streamline in the rotating frame of reference in the bulk but interrupted near the free surface by small trajectory segments on the cylindrical surface $r = R^*$ which result from their particle-motion model. The closed particle trajectory, interpreted as PAS, was found to be located in the immediate vicinity of, but generally distinct from, a closed streamline in the steady flow representing the traveling hydrothermal wave in the rotating frame of reference. In their model they also found particle accumulation on small closed toroidal tubes. For that reason they distinguished between *linelike* PAS (for the perfect and sharp accumulation along a line) and *tubular* PAS. Tubular PAS would visually appear as a significantly widened PAS string where the particle density on the skin of the tube is higher than in the interior of the tube. In their work, Hofmann and Kuhlmann [13] have provided evidence that the particle-accumulation phenomenon

*roman.mukin@tuwien.ac.at
†h.kuhlmann@tuwien.ac.at

is closely related to the topology of the three-dimensional flow field. However, they could not numerically resolve the flow field to such a degree that the particle trajectories could be accurately predicted over a sufficiently long period of time. The concept of PAS has been further generalized by Muldoon and Kuhlmann [14] by introducing *strange* PAS, in which particles are attracted to a complex subspace of the liquid bridge which results from the particle motion model and which resembles a strange attractor.

In the mathematical model of point particles which behave as tracers, and thus perfectly follow an incompressible flow, particles cannot accumulate. In order for dissipative structures of real particles to exist (e.g., in the form of a limit cycle) in an incompressible flow, the motion of real particles must deviate from the motion of perfect tracers (fluid elements). Such deviations can be considered to be dissipative perturbations of the undisturbed (conservative) motion of ideal tracers. The weak dissipation governing the motion of real particles can be of different types. Several authors [15–17] have claimed that Stokes drag as given by the Maxey-Riley [18] or the inertial equation [19,20] causes PAS. However, since the drag effect for the Stokes numbers in question is very small in the bulk, in particular for density-matched particles for which PAS form most easily, we follow the idea of Hofmann and Kuhlmann [13] that the dissipation for the particle motion primarily arises where the flow is fast and the shear gradients are high. These conditions are only met in the thin thermocapillary boundary layer of the free surface. Therefore, a particle which nearly perfectly follows the flow in the bulk will experience a certain streamline hopping or streamline mapping during its motion in the thin layer immediately below the free surface. In view of the enormous numerical effort to solve the fully coupled problem on scales well below the particle size it is of considerable interest to study such a streamline mapping in the dissipation zone near the free surface and to investigate the implications on the motion of otherwise passively advected particles. To accomplish this task, the flow field of the hydrothermal wave must be sufficiently resolved, much better than that by Hofmann and Kuhlmann [13], because tracking particles in the discrete Navier-Stokes flow field is much more demanding than computing particle trajectories in certain model flows which are accurately known up to machine precision [14,21]. Finally, the dissipative effect of a non-volume-preserving flow-field interpolation and also the dissipation of certain low-order time integrators can fake particle accumulation structures which are very similar to the ones observed experimentally [22].

Since the flow structure is an important factor for PAS, we shall investigate the topology of hydrothermal waves. This is not only interesting from the point of view of PAS (de-mixing of particles) but also in the more general context of mixing (of liquids or liquid-suspended particles). It is well known that incompressible steady three-dimensional flows allow for regular and chaotic streamlines [23]. Most studies of mixing have been carried out for two-dimensional unsteady incompressible laminar flows which were periodically driven (see, e.g., Refs. [24–26]) or for three-dimensional Stokes flows (see, e.g., Refs. [27–29]). While experimental investigations on mixing in three-dimensional flows are available [30,31] numerical work on mixing in three-dimensional laminar flows are sparse, in particular for time-dependent three-dimensional flows.

The topology of hydrothermal waves [32] is conveniently investigated in the frame of reference corotating with the wave, as the flow field is steady in this frame of reference. Hydrothermal waves arise from a linear instability of the axisymmetric toroidal basic flow on an increase of the Reynolds number. For high Prandtl numbers, a pair of azimuthally counterpropagating waves bifurcate from the basic state via a Hopf bifurcation [33,34]. For slightly supercritical flow conditions the time-asymptotic state appears as an azimuthally traveling hydrothermal wave if the Prandtl number is moderately large, whereas azimuthally standing hydrothermal waves emerge for long times if the Prandtl number is very large [35].

Here we consider hydrothermal waves for a Prandtl number of $\mathrm{Pr} = 4$, because the analysis is not made difficult by exceedingly thin velocity and temperature boundary layers. Moreover, we consider a length-to-radius ratio of $\Gamma = d/R = 0.66$ as in Hofmann and Kuhlmann [13], because it is known that PAS with azimuthal wave number $m = 3$ can safely be established experimentally for this aspect ratio. After a mathematical definition of the flow system we present the numerical solution methods and a code validation. Thereafter, we discuss the flow topology for several Reynolds numbers. After introducing a dissipation model for the particle motion we consider its effect on the particle transfer between streamlines, i.e., the corresponding streamline mapping. The properties of the mapping will be discussed. Finally, the results are summarized.

II. FORMULATION OF THE PROBLEM

We consider the incompressible flow of a Newtonian liquid with kinematic viscosity ν in a liquid bridge of length d which is suspended between two coaxial cylinders of radius R. In the limit of large mean surface tension and under zero-gravity conditions the equilibrium shape of a liquid bridge with a volume $\pi R^2 d$ is an upright cylinder if the bounding disks are parallel and concentric. For fixed contact lines and $d < 2\pi R$ this equilibrium shape is stable [36–38]. We use cylindrical coordinates with the origin in the midplane of the liquid bridge. The motion in the liquid bridge is driven by thermocapillary stresses along the free surface which are due to surface-temperature variations induced by keeping the supporting coaxial cylindrical rods at constant temperatures differing by ΔT. If we assume constant material parameters and the absence of gravity the fluid motion is governed by the Navier-Stokes, continuity and energy equations

$$\begin{aligned} \frac{\partial \vec{u}}{\partial t} + \vec{u}\cdot\nabla\vec{u} &= -\nabla p + \nabla^2\vec{u}, \\ \nabla\cdot\vec{u} &= 0, \\ \frac{\partial T}{\partial t} + \vec{u}\cdot\nabla T &= \frac{1}{\mathrm{Pr}}\nabla^2 T, \end{aligned} \tag{1}$$

where the equations have been made dimensionless using the length scale d, the time scale d^2/ν, the velocity scale ν/d, the pressure scale $\rho\nu^2/d^2$, and the temperature scale ΔT. Such viscous-diffusive scaling has also be used by, e.g., the authors of Refs. [6,39]. The geometry is characterized by the aspect

ratio $\Gamma = d/R$, and $\mathrm{Pr} = \nu/\kappa$ is the Prandtl number, where κ is the thermal diffusivity.

On the rigid walls we impose constant-temperature and no-slip boundary conditions. The free surface is assumed to be adiabatic and to support thermocapillary stresses such that

$$\begin{aligned} \vec{t}\cdot\mathsf{S}\cdot\vec{n} + \mathrm{Re}\,\vec{t}\cdot\nabla T &= 0, \\ \vec{n}\cdot\nabla T &= 0, \end{aligned} \tag{2}$$

where $\vec{n}$ is the unit normal vector to the free surface directed out of the liquid, $\vec{t}$ any of the two orthogonal tangent vectors and $\mathsf{S} = \nabla u + (\nabla u)^{\mathrm{T}}$ the viscous part of the dimensionless stress tensor. The thermocapillary Reynolds number is $\mathrm{Re} = \gamma \Delta T d/\rho\nu^2$, where γ is the negative surface-tension coefficient. In this study we consider Prandtl number $\mathrm{Pr} = 4$ and aspect ratio $\Gamma = 0.66$.

III. NUMERICAL MODELING

A. Flow simulation

The numerical simulations are performed using the open-source CFD package OPENFOAM [40]. OPENFOAM uses a control-volume-based technique to solve the governing system (1) together with the boundary conditions (2) on a hexahedral, nonuniform, and unstructured mesh shown in Fig. 1.

The flow-field variables are defined on a collocated grid. The numerical solution is obtained by the pressure-implicit with splitting of operators (PISO) algorithm for the pressure-velocity coupling, implemented according to the Rhie-Chow type of interpolation.

All convective terms are approximated by a central-difference scheme. All inviscid terms and the pressure gradient were approximated with fourth-order accuracy. A second-order backward-Euler differentiation method was used for the time integration together with a dynamically adjustable time-stepping technique to guarantee a local Courant number of less than 0.5. A preconditioned biconjugate gradient (PBiCG) method with incomplete Cholesky preconditioner was used for solving the resulting linear systems with a local accuracy of 10^{-8} for all dependent variables at each time step. Using the PBiCG method together with incomplete Cholesky preconditioner increases the scalability of the algorithm, particularly for a large number of control volumes.

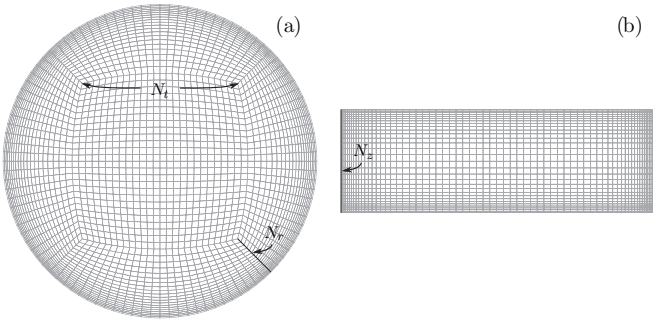

FIG. 1. (a) Axial view of the mesh. (b) Lateral view of the mesh. Only every fifth grid line is displayed.

B. Grid refinement study

The computations have been performed on nonuniform grids. The grids are characterized by the number N_t of collocation points in both lateral directions in the core region, the number N_r of grid points in the radial direction adjacent to the free surface, and the number N_z of cells in the axial direction. The grid has been compressed near the free surface and the bottom and the top rods in order to resolve the high gradients near the cold and hot corners of the liquid bridge. The resolution of the flow field in these parts of the liquid bridge plays a crucial role in the computations, since Marangoni boundary layers arise in the two corner regions. The scaling of the boundary layers for high-Prandtl-number liquids was studied in detail by Cowley and Davis [41] for the hot-corner region and by Canright [42] for the cold-corner region. The large gradients of the velocity and the temperature in these regions are caused by the thermocapillary forces acting on the free surface (see, for example, Ref. [43]).

The simulations are initiated from a state of rest and a homogeneous mean temperature, i.e., $\vec{u}(t=0) = 0$ and $T(t=0) = 0$. The integration was carried out on a relatively coarse grid (case 1 in Table I) until a toroidal vortex flow was established. At a time t^* the temperature field was disturbed by adding a disturbance-temperature field $T'(r,\varphi,z,t^*) = (A\Gamma r)\sin[\pi(z+1/2)]\sin(m\phi)$ with a small perturbation amplitude $A = 0.025$ and azimuthal wave number $m = 3$. This type of perturbation is invariant with respect to reflections of φ and will thus evolve into a time-dependent flow whose frequency spectrum is mirror symmetric with respect to the frequency $\omega = 0$ of the hydrothermal wave, i.e., the flow will evolve into a standing wave. For $\mathrm{Pr} = 4$ and slightly supercritical conditions, Leypoldt *et al.* [34] has shown that the standing wave is unstable and decays to a traveling hydrothermal wave (see also Ref. [35]).

The time dependence of the Nusselt-number difference between the hot and the cold walls $\Delta\mathrm{Nu} = 2(\mathrm{Nu_{top}} - \mathrm{Nu_{bot}})/(\mathrm{Nu_{top}} + \mathrm{Nu_{bot}})$ as well as the free-surface temperature at midplane at $\varphi = 0$ are shown in Fig. 2 for $\mathrm{Re} = 1800$. The transition from a standing wave to a traveling wave can be seen at about $t \approx 13$. After a traveling hydrothermal wave has developed and the Nusselt numbers at the solid walls have become stationary the computation was terminated. The hydrothermal wave obtained on the coarse grid was, thereafter, interpolated to a fine grid and the fine-grid interpolant was relaxed by time integration until a fully developed hydrothermal wave was obtained.

To prove grid convergence we consider the angular velocity Ω of the hydrothermal wave and the Nusselt number at the bottom wall. Both quantities are time independent in the traveling-wave state. Moreover, the angular velocity is an important scalar and the Nusselt number $\mathrm{Nu_{bot}}$ is a sensitive quantity, as the largest temperature gradients arise near the cold corner. Table I provides the computed angular velocity Ω and the bottom-wall Nusselt number $\mathrm{Nu_{bot}}$ for different grids.

Doubling the number of cells from about 1 to 2 million yields a reduction of Ω by $\approx$0.1%. An increase of the number of cells to about 4 million yields a further decrease by $\approx$0.1%. The change of the frequency by an increase of the number of cells from 9 to about 16 million is below 0.001%. While the

TABLE I. Azimuthal velocity $\Omega = \omega/m$ ($m = 3$) of the fully developed traveling hydrothermal wave as function of the grid size for Re = 1800. The minimum linear dimension over all cells is specified by δ. N_t, N_r, and N_z denote parameters of the computational mesh, except for the result of Hofmann and Kuhlmann [13], where N_t, N_r, and N_z correspond to the number of cells in azimuthal, radial, and axial directions, respectively.

			No. cells				
Ω	$\mathrm{Nu_{bot}}$	δ	N_t	N_r	N_z	Total no. cells	Case/authors
10.142		1.1×10^{-3}	32	100	66	211 200	[13]
10.121	3.9907	2×10^{-3}	100	68	66	1 149 120	1, present
10.113	3.9879	9.1×10^{-4}	120	80	80	2 257 600	2, present
10.103	3.9871	6.8×10^{-4}	144	96	94	3 840 000	3, present
10.101	3.9864	2.5×10^{-4}	160	108	106	9 192 960	4, present
10.101	3.9861	1.2×10^{-4}	200	135	132	15 925 248	5, present

accuracy of Ω is certainly sufficient for most purposes, we need this accuracy in order to resolve very fine flow structures which will be unraveled by following the motion of substantial fluid elements for a long time. Therefore, the flow field obtained on the finest grid (15 925 248 cells) was used for all subsequent calculations.

C. Accuracy of computed streamlines

The topological properties of a flow can be studied by the motion of fluid particles, i.e., by a Lagrangian representation of the fluid elements. The position $\vec{X}(t)$ of a fluid particle, or a perfect tracer, initially velocity matched to the flow is governed by

$$\frac{d\vec{X}}{dt} = \vec{u}(\vec{X}), \quad \vec{X}(t=0) = \vec{X}_0, \tag{3}$$

where $\vec{X}_0$ is the initial location of the fluid element. Using the phase velocity of the hydrothermal wave, the flow originally obtained in the laboratory frame of reference is transformed into the rotating frame or reference. As (3) remains form invariant under this transformation, (3) is solved using the steady three-dimensional flow in the rotating frame of reference.

Equation (3) is integrated by a sixth-order Runge-Kutta method using a time step $\Delta t = 10^{-6}$, in which point weighted interpolation functions were used to obtain the velocity field at arbitrary intergrid points. The interpolation functions used depend on the cell type (for details, see Ref. [44]). While

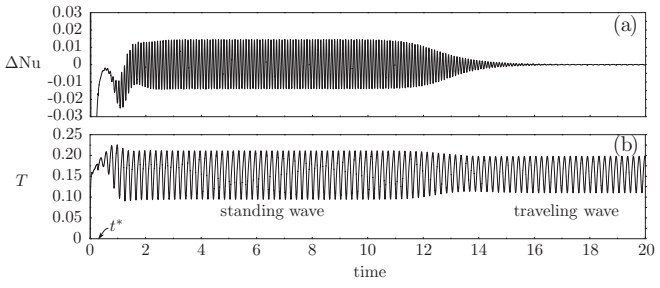

FIG. 2. (a) Temporal evolution of ΔNu for Re = 1800. (b) Time dependence of the free-surface temperature at midplane $(r,\varphi,z) = (R,0,0)$. The three-dimensional perturbation was imposed at t^* as indicated.

chaotic trajectories can be predicted only for a limited time, nonchaotic trajectories can be computed for a much longer time. Nevertheless, error accumulation can occur [22]. However, for the integration times used in this work ($t \leqslant 10$), the error accumulation due to the discretization in time turned out to be negligible compared to the discretization error in space. Tests have shown, moreover, that for this period of time chaotic trajectories also can be predicted with sufficient accuracy.

Since the error associated with interpolation of the discrete solution of the Navier-Stokes equations cannot readily be assessed, we considered the analytical model of Kuhlmann and Muldoon [21]

$$\vec{u} = \begin{pmatrix} u \\ v \\ w \end{pmatrix} = \begin{pmatrix} -\pi A_0 r^n (1-\Gamma r)\sin(\pi z) + r^k (1-\Gamma r) A_1 \sin(m\varphi) \\ -[\Gamma(k+2)r^{k+1} - (k+1)r^k](A_1/m)\cos(m\varphi) - \Omega r \\ A_0[\Gamma(n+2)r^n - (n+1)r^{n-1}]\cos(\pi z) \end{pmatrix}, \tag{4}$$

where (u,v,w) denote the radial, azimuthal, and axial components of the velocity field. We use the parameters $m = 3$, $n = 4.74$, $A_0 = 11.1$, $k = 1.5$, $A_1 = 11.3$, and $\Omega = 10.1$ which were also used by these authors. The flow field is a semiquantitative model for a hydrothermal wave in the rotating frame of reference. It is exactly incompressible and known to machine precision at any point.

To assess the error associated with the flow-field interpolation which is required when computing a Lagrangian path in a discrete flow field we discretized (4) to an unstructured grid comparable to the one used for the Navier-Stokes simulations and interpolated the discrete values. Since the spatial discretization error can be regarded as a dissipative perturbation of the exact volume preserving flow field (4), we expect that any closed orbits (elliptical points in a Poincaré section) transform to limit cycles in the discretized and interpolated system (sinks or sources in a Poincaré section). Figure 3 shows a comparison between the trajectory of a fluid element in the exact analytical flow field (4) with the trajectory obtained by a discretization on several grids. For the finest grid the difference between the trajectories computed with and without interpolation at $t = 50$

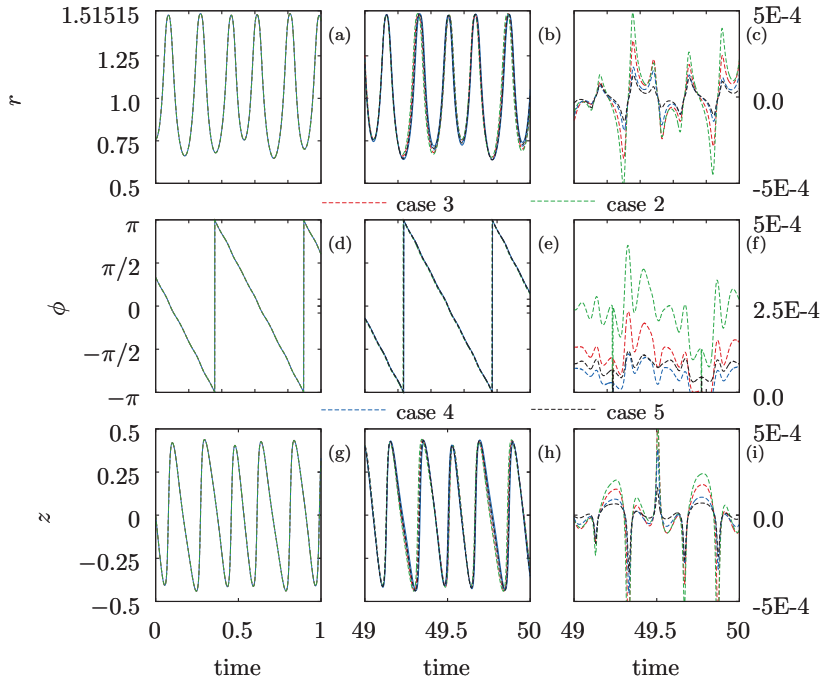

FIG. 3. (Color online) Comparison of Lagrangian trajectories using the continuous flow (4) (blue solid line) and discretizations of (4) (dashed lines) on the grids presented in Table I: case 2 (green dashed line), case 3 (red dashed line), case 4 (blue dashed line), and case 5 (black dashed line). The difference between the solutions obtained using a discrete flow and by using the continuous flow (4) is shown in the right column for the period $t \in [49,50]$. The initial condition is $(r_0,\varphi_0,z_0) = (0.75,\pi/3,0)$. The trajectory is regular.

is of the order of 5×10^{-4}. This small deviation is more than sufficient to reliably compute regular trajectories up to $t = 10$ using an interpolation of the discretized flow field (4). Due to the similarity we expect a similar accuracy for the interpolation of the discrete Navier-Stokes flow.

IV. RESULTS

A. The flow field

As a representative example we show in Fig. 4 the azimuthal velocity and the temperature field of the fully developed hydrothermal wave for $\mathrm{Re} = 1800$ in the midplane $z = 0$ of the liquid bridge in the laboratory frame of reference. The azimuthal wave number is $m = 3$ and the spiral pattern of the isolines of the azimuthal velocity v is easily recognized. The torsion of the flow pattern is characteristic for a hydrothermal wave propagating in a clockwise direction [33,45]. In Fig. 4(b) high-temperature gradients are visible near the free surface (Marangoni boundary layer) as well as in the interior. The hydrothermal wave receives its energy from the latter gradients [33,46]. Figure 5 shows isolines on the free surface at $r = R$ of the axial and azimuthal velocity as well as the temperature field. The hot- and cold-wall boundary layers of the temperature field are visible by the crowding of isotherms at the top and bottom of the lower figure. These wall layers are most pronounced near the cold and hot corners.

The topology of the hydrothermal wave is most conveniently studied in the rotating frame of reference in which the wave is steady. The flow in the rotating frame is readily obtained by a single snapshot only of the fully developed hydrothermal-wave state $\vec{u}(\vec{x},t)$ and by subtracting the solid body rotation $\Omega r \vec{e}_\varphi$ associated with the phase speed $\Omega = \omega/m$ of the wave, where ω is the oscillation frequency of the wave. Streamlines in the rotating frame of reference are then

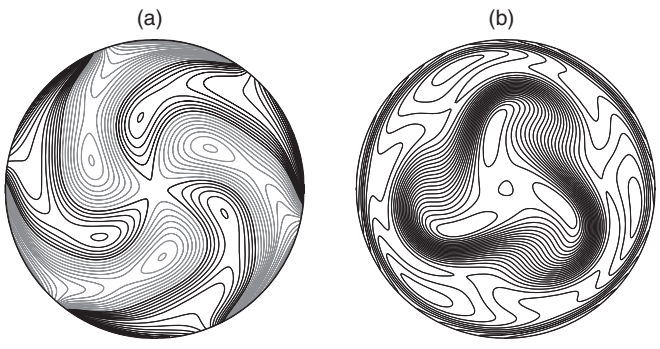

FIG. 4. Equidistant isolines of the azimuthal velocity (a) in the laboratory frame of reference and of the temperature field (b) at midplane $z = 0$ for the fully developed clockwise-traveling hydrothermal wave for $\mathrm{Re} = 1800$. Gray isolines indicate negative values.

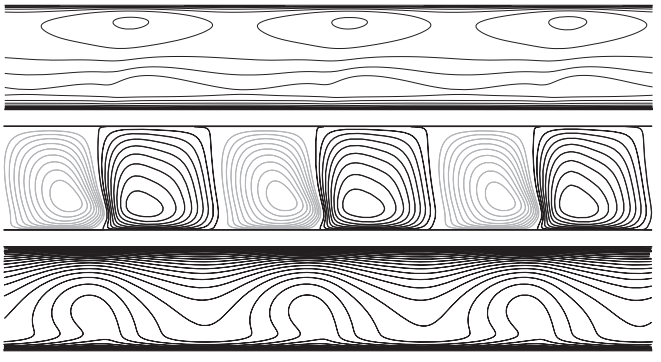

FIG. 5. Isolines of the axial velocity (top), the azimuthal velocity (middle), and the temperature field (bottom) on the free surface unwrapped from 0 to 2π for $\mathrm{Re} = 1800$. The hydrothermal wave travels from right to left and is displayed in the laboratory frame of reference.

obtained by Lagrangian trajectories of fluid elements. This saves enormous amounts of computing time, because the flow field must not be simulated along with the Lagrangian trajectories as was done by other investigators (see, e.g., Ref. [47]). Moreover, the interpretation of trajectories in a steady flow is much easier than in a time-dependent flow field.

B. Regular and chaotic streamlines

From the theory of dynamic systems a necessary condition for the existence of chaotic advection is that the flow should be either three dimensional or two dimensional and time dependent. The most common approach for a detection and characterization of chaotic advection is the tracking of numerous fluid elements for long times. Here we shall use Poincaré sections to determine whether the motion of a given fluid particle is chaotic or regular.

We consider the flows for three Reynolds numbers, Re = 1800, 2600, and 3000. The angular velocities of the hydrothermal waves are $\Omega = 10.101$, 12.210, and 13.092, respectively. The Poincaré sections in the midplane $z = 0$ shown in Fig. 6 have been obtained by computing trajectories of a large number of fluid elements up to $t = 10$. The initial conditions were equidistantly distributed on a circle about the vertical axis in the midplane. Whenever a trajectory crosses the midplane $z = 0$ the intersection point is marked. The trajectories of the fluid elements are streamlines in the rotating frame of reference. If the Poincaré points are scattered irregularly we conclude that the corresponding streamlines are chaotic. In all three Poincaré sections of Fig. 6 several distinct open patches can be seen. These blank regions are the isolated regular islands. The region outside of these islands is the chaotic sea. Even though the Poincaré points in the chaotic sea seem to be dense, it is possible to find some very small isolated regular islands. As a general property of steady incompressible flows with chaotic streamlines, the trajectories of fluid particles in the chaotic sea can never enter any regular island (blank patches), and neither can regular trajectories inside a regular island ever reach the chaotic sea.

In the following, we focus on the streamlines in the regular regions of the flow, i.e., the streamlines inside of the blank islands in Fig. 6. If the starting point of a fluid element will be inside of a regular region the trajectory of this fluid element will lie on a torus. The torus is a closed stream tube in the rotating frame of reference. All such tori are also called Kolmogorov-Arnold-Moser (KAM) surfaces. The KAM tori arise in different sets. Within each set the tori are nested and isolated from the outside flow and from each other. Each KAM torus contains at least one central closed streamline which can be recognized as a fixed point in the Poincaré section. To visualize and characterize the largest and, hence, the most significant KAM surfaces, we identified by visual inspection the largest KAM surfaces. As the structure of the KAM tori is generally very complex and extends to scales which cannot be resolved by the present method, these visualizations are approximations only.

The dominant KAM surfaces are shown in Fig. 7. For all Reynolds numbers considered by far the largest closed streamtube is a remnant of the strong axisymmetric basic flow which is underlying in the total flow field. We shall call this KAM surface the toroidal core T_{core} (shown in red). Practically all other closed streamlines and closed tubes wind about the toroidal core and we shall distinguish them using the notation T_i^j introduced by Kuhlmann and Muldoon [14,21], where i is the fundamental azimuthal wave number of the KAM torus and j is the number of revolutions the particular tube makes per azimuthal period 2π. The closed trajectories inside the tubes shall be denoted L_i^j, correspondingly. In addition to the core, Fig. 7(a) for Re = 1800 shows T_3^3 (blue) and T_3^6 (green). T_{core} and T_3^3 have been identified before by Hofmann and Kuhlmann [13]. However, the resolution of the flow field obtained by these authors was too low to reconstruct these tori in three dimensions. With the present resolution, we have been able to resolve also T_3^6. The closed streamlines L_3^3 and L_3^6 have also been found by Hofmann and Kuhlmann [13]. As the Reynolds number increases we find that the tori T_3^3 and T_3^6 become thinner. In fact, we no longer could find the KAM surface for T_3^6 for Re = 2600. However, we find another dominant KAM surface T_3^9 (yellow) which is tightly wrapped about the core.

Figure 8 shows the fine structure of the dominating winding KAM torus T_3^3 for Re = 1800 in the plane $z = 0$ by zooming in. It can be seen that more than one closed streamline exists

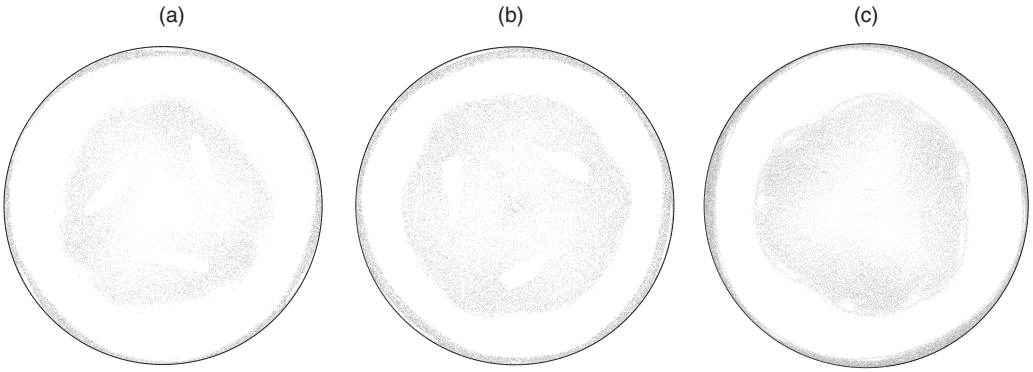

FIG. 6. Poincaré sections at the midplane of the liquid bridge for (a) Re = 1800, (b) Re = 2600, and (c) Re = 3000. The Poincaré points have been obtained from trajectories of 1000 fluid elements initially placed on the circle $(r_0, z_0) = (R - \delta, 0)$ one grid point below the free surface, where $\delta = 1.2 \times 10^{-4}$ is the minimum radial grid size in Table I (for the finest grid resolution). Trajectories have been calculated for the period $t \in [0,10]$. The bounding circle indicates the free surface.

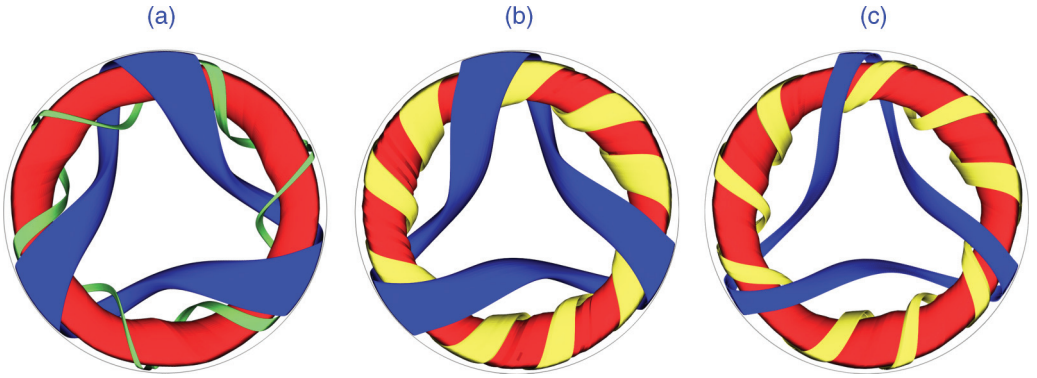

FIG. 7. (Color online) Dominant KAM tori for Re = 1800 (a), Re = 2600 (b), and Re = 3000 (c). The tori are indicated by [color (grayscale)] as follows: [blue (very dark)] T_3^3, [red (dark)] T_{core}, [green (bright)] T_3^6, and [yellow (very bright)] T_3^9. The gray circle indicates the free surface.

inside the outermost KAM tori, which are shown in red. There exist further independent sets of KAM tori imbedded in T_3^3 which also accommodate closed streamlines. The tubular structures of the subsets shown in olive and blue have been resolved but we could not resolve the fine structure of the red Poincaré points. Figure 9 shows examples for KAM tubes $T_{1a,b}^8$, T_3^9, and T_{1a}^{10} for Re = 1800. All these KAM tori are embedded in the core T_{core} (not shown).

From the analysis of the Poincaré sections and the reconstructed KAM tubes (Figs. 6 and 7) we find the tendency that the regular regions shrink upon an increase of the Reynolds number and may eventually vanish completely. As a result, the chaotic sea is increased with increasing Reynolds number. Another feature of interest is the minimum distance of the KAM tori and the closed streamlines from the free surface. We find that the distance of T_3^3 from the free surface shrinks as the Reynolds number increases (see Table II). The significance of the minimum distances between the KAM tori and the free surface will be discussed in Sec. IV D.

C. Particle motion

1. Significance of the particle–free-surface interaction

In order to model the particle motion in the flow field computed numerically, we first consider the experimental facts. From previous experimental investigations the following unique features of PAS can be extracted.

(1) Under optimum conditions the formation of linelike PAS from a random particle configuration is very rapid, even more rapid than the formation of a traveling hydrothermal wave from a disordered flow state: Once a hydrothermal wave is formed PAS arises almost immediately [48].

(2) The formation time of PAS is minimized if the particles are neutrally buoyant [11].

(3) Besides of PAS in form of a thin closed thread, quite a number of particles remain well mixed in a toroidal core [9], even for relative particle density of $\rho_p/\rho_f = 1.7$ [49].

(4) Particles on PAS are moving extremely close to the free surface. Tanaka *et al.* [9] state, "According to the observation by a high speed CCD camera, the clearance between the free surface and the particles is never larger than half a diameter of the particle." Hence, the minimum film thickness between the surface of the particles on PAS and the free surface has been found to be safely less than one particle radius. This agrees with the observations of Ueno *et al.* [48].

(5) The existence, shape, and formation time of PAS depend strongly on the size of the particles [11].

(6) Particles are depleted from the center of the liquid bridge even at relatively low Marangoni numbers [50–52].

From (1) we conclude that there exists a very strong dissipative process for the particle motion that quickly leads to PAS. The observation (2) shows that the key dissipative mechanism for the particle motion does not depend on the density difference between particles and liquid. The existence

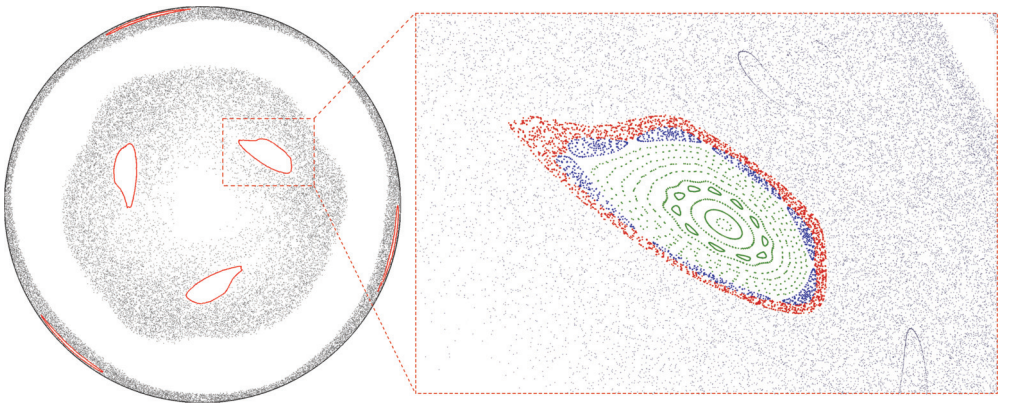

FIG. 8. (Color online) Zoom into the dominant winding stream tube T_3^3 for Re = 1800.

FIG. 9. (Color online) Examples for KAM tubes with larger winding numbers for Re = 1800: $T^8_{1a,b}$ [red (dark)], T^9_3 [yellow (bright)], and T^{10}_{1a} [cyan (medium gray)]. The circle indicates the free surface.

for a time much larger than the PAS formation time of a core of particles even for heavy particles with $\varrho = 1.7$ (3) proofs the weak effect of inertia for the particle sizes used in the experiments. According to Ueno [53], "a toroidal core of particles is always observed in addition to linelike PAS in the experiments using particles with diameter of 5 to 30 microns and particle densities in the range of 1.5 to 2×10^3 kg/m^3 (the density of 2 cSt silicone oil at 25 °C is 0.873×10^3 kg/m^3)." Obviously, the experimentally observed core of particles corresponds to the KAM torus T_{core} and KAM tubes in the close vicinity of T_{core} [49]. From these observations, the key process leading to PAS cannot solely be the dissipation due to Stokes-drag forces for the Stokes numbers encountered in the experiments (see also Ref. [21]). Schwabe *et al.* [11] did not report a core of particles, because their experiment with $NaNO_3$ as a liquid was run for hours, a time by which even minute centrifugal effects will have removed all particles from the core [54].

Observations (4) to (6) give indications as to the source of the strong dissipation. Since PAS come very close to the free surface (4) the particles enter a region of rapid flow and high shear; moreover, the presence of the free surface will affect the particle motion close to it. This condition alone suggests that the dissipation for the particle motion is much higher in the free-surface shear layer than in the bulk (see, e.g., Ref. [55]). Furthermore, the strong dependence of PAS on the particle size (5) indicates that the length scale of the particles matters. The only length scale that linelike PAS has in common with the particle size is its distance from the free surface. Therefore,

TABLE II. Characteristic distances of the separating KAM torus for the dominant regular structures.

Re	KAM system	$\Delta_{\min}$	Δ_L	Δ_p
1800	T^3_3	0.0075	0.01325	0.02117
2600	T^3_3	0.005625	0.017164	0.0345
3000	T^3_3	0.00514		0.0295

the dissipative effect on the particle should depend on the distance from the free surface. This conclusion is further supported by observation (6): The experiments show that particles are rapidly expelled from the near-axis region, even for very small particles (see also Ref. [14]). The streamlines in the central region, however, are those which approach the free surface the closest. Hence, particles moving on trajectories which are similar to these streamlines will approach the free surface the closest.

2. *Dissipation model for the particle–free-surface interaction*

For the above reasons there is ample experimental evidence for a strong dissipation which acts only on a small length scale from the free surface which is comparable to the size (radius) of a spherical particle. The motion of the particles near the free surface is important because of the extreme crowding of streamlines and because the free surface expands near the hot wall and contracts in the middle of the liquid bridge, due to the acceleration and deceleration of the liquid directly at the interface. The divergence of the surface flow caused by the acceleration and deceleration promotes particles to make contact to and be released from the free surface, respectively. To model the dissipation we adopt the inelastic hard-wall model of Hofmann and Kuhlmann [13] applied to all boundaries. At the free surface the motion of the center of a spherical particle is restricted to $r < R^*$ with $R^* = R - \Delta$. The hard-wall model is thus characterized by a single parameter Δ only. It will depend both on the flow field and the particle size. It is expected that Δ is slightly less than the particle radius with $\Delta = a$ in case the particles make contact with the free surface. The same model has also been employed by Kuhlmann [21] and Muldoon [14].

The effect of the hard-wall potential on the motion of a model particle is equivalent to a mapping among streamlines on which the model particles move: a streamline intersecting the cylinder $r = R^*$ in a point in which the radial velocity $u|_{r=R^*} > 0$ (particle colliding with the hard-wall) will be mapped to another streamline on which the particle moves after the interaction process. The streamline to which the intersecting streamline is mapped satisfies the release condition $u|_{r=R^*} = 0$ on R^* with $\partial u/\partial s|_{r=R^*} < 0$, where s is the arclength along the streamline, i.e., this streamline is tangent to R^* in a point, the release point. Typically, the union of release points is a closed curve on $r = R^*$ which is called the release line z_R. Depending on the flow field, there may be more than one release line.

The effect of the streamline mapping is illustrated in Fig. 10 for the two-dimensional basic flow at Re = 1000, close to the onset of hydrothermal waves. In the two-dimensional flow the particle free-surface interaction will lead to an axisymmetric toroidal shell as was observed in the experiments of Schwabe and Frank [56] and Schwabe and Mizev [57].

D. Streamline mapping near the free surface

1. *General properties*

The parameter Δ together with the flow topology determines the properties of the streamline mapping and the structure of the resulting attractors. In order for streamlines to be mapped (particles to be transferred) to a particular KAM

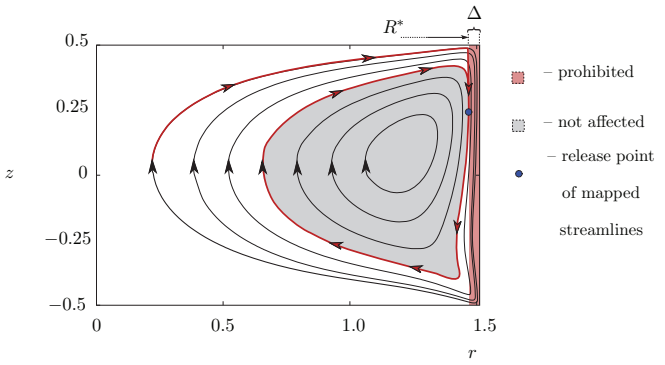

FIG. 10. (Color online) Streamlines of the two-dimensional steady flow in a liquid bridge with Pr = 4 and $\Gamma = 0.66$ for Re = 1000. The particle–free-surface interaction in a subsurface layer of thickness Δ [red (dark gray)] prevents particles from following the streamlines near the free surface. Particles moving on streamlines in the light gray region are not mapped. Particles moving on streamlines in the white region are mapped to the release point [blue (dark gray)].

torus, this KAM torus must necessarily intersect the release line. Since the release line lies on R^*, this condition requires (a) an intersection of the outermost KAM torus which separates the regular from the chaotic region (separating KAM torus) with R^* and (b) a line segment of the release line must lie inside of the the intersecting set of tori.

Different cases can arise depending on $\Delta \lessgtr \Delta_L$, where Δ_L is the distance of the central closed streamline L_i^j of the set of KAM tori from the free surface and on the width of the separating KAM tube. The sketches in Fig. 11 show the typical cases in a horizontal plane near the point of closest approach of L_i^j to the free surface. The release line lies approximately in the same plane.

(a) If Δ is so small that the separating KAM torus does not intersects R^* the streamlines inside of this KAM torus (small dots) are undisturbed and experience no mapping. Hence, particles on these KAM tori are advected undisturbed, i.e., they continue to move on one and the same torus. This is typically the case for the toroidal core, T_{core}, because its KAM torus remains sufficiently far from the free surface.

(b) In the limiting case only the separating KAM torus is tangent to $r = R^*$.

(c) If only a few KAM tori of a set intersect R^* the streamlines inside of the KAM torus which is tangent to R^* in one point remain unaffected, while all streamlines of the outer KAM tori are mapped, because they intersect $r = R^*$. This is the case for tubular PAS (introduced by Ref. [13]) in which particles are transferred to the KAM tube tangent to R^*.

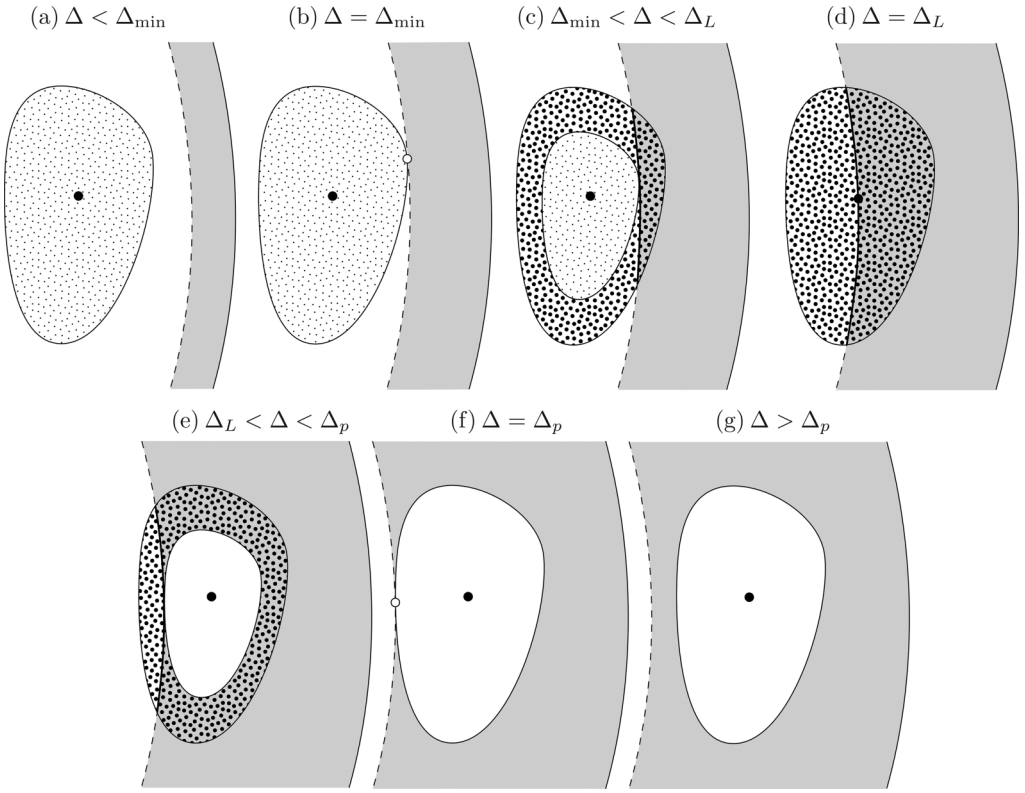

FIG. 11. Schematic representations of cross sections through the separating KAM torus in horizontal planes for different values of Δ. In each plane the particular KAM torus tangent to R^* has reached its maximum radial extension. The gray area indicates the annular volume of radial thickness Δ between R^* (dashed arc) and R (solid arc) which is unaccessible for model particles due to the hard-wall interaction at $r = R^*$. The outer oval indicates the contour of the regular region (separating KAM torus). The area filled with small dots represents the set of KAM tori on which particles move without any free-surface interaction. The white ovals represent those KAM tori which become depleted of particles. The area filled with the larger dots indicates KAM tubes to which streamlines are mapped (particles are transferred). The thick arc on R^* inside the regular region indicates the segment of the release line inside the regular region. The large dot indicates the closed streamline L_i^j and the open circles represent the points at which the separating KAM torus becomes tangent to $r = R^*$ (first contact point and pinch point).

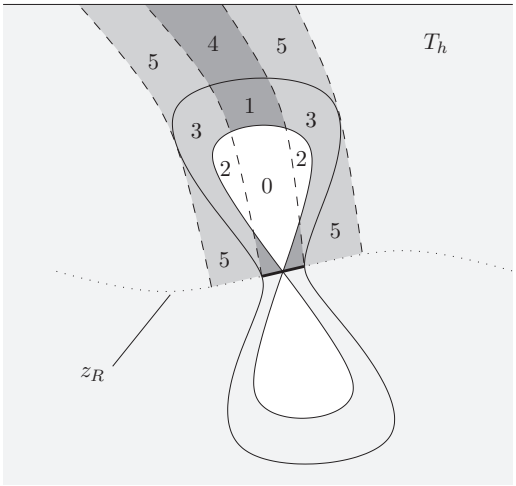

FIG. 12. Schematic representation of the intersection of the separating KAM tube T_i^j (outer oval contour) on the unwrapped cylinder $r = R^*$ [(r,φ) plane] close to pinching [Fig. 11(e)]. The dotted line is the release line z_R. The inner KAM tubes (white) do not receive particles and become depleted. The numbers indicate different mapping regions explained in the text. The dashed lines are streamlines of the restricted motion on R^*.

(d) If the central closed streamline L_i^j is tangent to R^* all streamlines of the KAM set of tubes are mapped.

(e) When the closed streamline intersects $r = R^*$ all streamlines of the set of KAM tubes experience a mapping, but all streamlines initially on the inner KAM tubes (white) which completely cross R^* will be mapped to the chaotic sea, because these KAM tubes will not intersect with the release line. The border between the tori whose streamlines are mapped to the chaotic sea and those being mapped to the regular region is made of the KAM torus tangent to R^* in one point. The inner KAM tori will be depleted of particles (see also Fig. 12), because they cannot receive any particles by the mapping as they are not connected with the release line.

(f) In the pinching limit, at $\Delta = \Delta_p$, the separating KAM tube intersects R^* as a whole being tangent to R^* in one point only. This is illustrated in Fig. 12 for a value of Δ slightly less than Δ_p at which pinching occurs.

(g) Finally, the KAM tube crosses R^* as a whole but does not intersect with the release line. Therefore, all particles of the regular region will be mapped to the chaotic region and the regular region becomes depleted of particles.

The contour on the cylindrical surface $r = R^*$ of the KAM tube separating the regular from the chaotic region is sketched in Fig. 12 just before pinching. The outer KAM tubes which can receive particles by release from the release line (thick solid line segment) are composed of regions 1 and 3. The two white areas denoted by 0 and 2 indicate the interior KAM tubes of the set which are not connected to the release line. Therefore, the interior tubes cannot receive particles. However, particles from this interior region will leave it, because all the interior streamlines are mapped elsewhere.

The mapping between streamlines corresponds to a restricted motion with $u = 0$ on R^*. A streamline intersecting with R^* at some point A is mapped to a streamline which is tangent to R^* in some point B on the release line. The two points A and B are connected by a streamline of the restricted two-dimensional motion on R^* which is given by $[v\vec{e}_\varphi + w\vec{e}_z]_{r=R^*}$. These lines, along which the mapping takes place, are indicated in Fig. 12 as dashed lines (in the rotating frame of reference). This geometrical consideration implies that the regular region receives particles by mapping from the regular regions 0 and 1 as well as from the chaotic region 4 (except possibly for a small region next to the hot wall where $w|_{r=R^*} > 0$). On the other hand, streamlines from the regular regions 2 and 3 are mapped to the chaotic region along the dotted part of the release line which lies in the chaotic sea. Chaotic streamlines from region 5 are mapped back to the chaotic sea. As the pinch point Δ_p is approached by increasing $\Delta \uparrow \Delta_p$ lesser streamlines are mapped to the regular region, because the segment of the release line inside of the separating KAM torus tends to zero. Beyond the pinch point, for $\Delta > \Delta_p$, streamlines are no longer mapped to the regular region. On the other hand, all streamlines from the regular region suffer a mapping to the chaotic sea. Therefore, all KAM tubes of the set will be depleted of particles.

2. *Mapping of streamlines for the Navier-Stokes flow at Re* = 1800

Different forms of PAS (linelike and tubular PAS) have been found for tracers of varying size in a moderately resolved Navier-Stokes flow [13] and in the closed-form model flow (4) [14] if a set of KAM tori intersects with the hard wall location such that a part of the release line is located within the regular region. In the framework of the current hard-wall model, the existence and the type of PAS for a given set of tori depends on three quantities of the regular regions as follows: (1) the minimum clearance $\Delta_{\min}$ between the free surface and the separating KAM torus [Fig. 11(b)], (2) the minimum clearance Δ_L between the free surface and the central closed streamline L_i^j [Fig. 11(d)], and (3) the maximum radial clearance R_m between the axis and the separating KAM torus which defines the pinch point $\Delta_p := R - R_m$ [Fig. 11(f)]. For the T_3^3 KAM system these data could be obtained with a reasonable accuracy. The corresponding interaction lengths are given in Table II. The characteristic distances for T_3^6 were very difficult to determine, due to the small size of these tubes. Moreover, the dominant T_3^3 KAM torus for Re = 3000 is found to be extremely squeezed and houses in its center one hyperbolic and two elliptic orbits (see Sec. V).

In the absence of a streamline mapping, for $\Delta = 0$, particles move as prefect tracers. In the following, we consider the streamline mapping for eight different interaction lengths from $\Delta = 0.005$ to $\Delta = 0.025$. The mapping is discussed by showing three-dimensional views of the KAM tubes relative to the surface $r = R^*$ and by displaying the release line on $r = R^*$ together with the contours of intersection with $r = R^*$ of the separating KAM tubes which separate the regular from the chaotic regions. We also show corresponding Poincaré sections at the midplane for 1000 representative fluid elements initially distributed all along the release line which experience a mapping or, equivalently, particles which experience a free-surface interaction. In addition, the configuration of 5000 model particles is shown at $t = 5$ which

were initiated at random in the whole volume $r \leqslant R^*$ and $|z| \leqslant z^* = 1/2 - \Delta$.

Figures 13(a), 13(c), 13(e), 13(g), 13(i), 13(k), 13(m), and 13(o) show the surface $r = R^*$ unwrapped from $\varphi = 0$ to 2π for the above mentioned set of Δ values. Gray lines represent the streamlines of the restricted two-dimensional motion on $r = R^*$ along which the three-dimensional streamlines are mapped. The direction of the restricted streamlines is from top to bottom. A subset of the mapped streamlines, originating from the release line z_R (red), reattaches to R^* at the reattachment line (blue), only to be released to the bulk a second time just before the cold wall. The arclengths of the reattachment lines decrease with increasing Δ and vanish for $\Delta \geqslant 0.025$. The reattachment is due to the shape of the streamlines of the basic flow near the free surface (cf. Fig. 10).

a. $\Delta = 0.005$ and $\Delta = 0.0075$. For $\Delta = 0.005$ there is a certain clearance between the regular region T_3^3 and R^* [Fig. 13(b)]; they are not intersecting. The same applies to T_3^6. Therefore, the streamline mapping only concerns chaotic streamlines. Typically, linelike PAS is absent in such a case. For $\Delta = 0.0075$ the clearance between $r = R^*$ and the T_3^3 KAM surface is very small; they almost touch [Fig. 13(d)]. Again, only chaotic streamlines are mapped. However, a range of the chaotic target streamlines (tangent to R^* at z_R) for $\Delta = 0.0075$

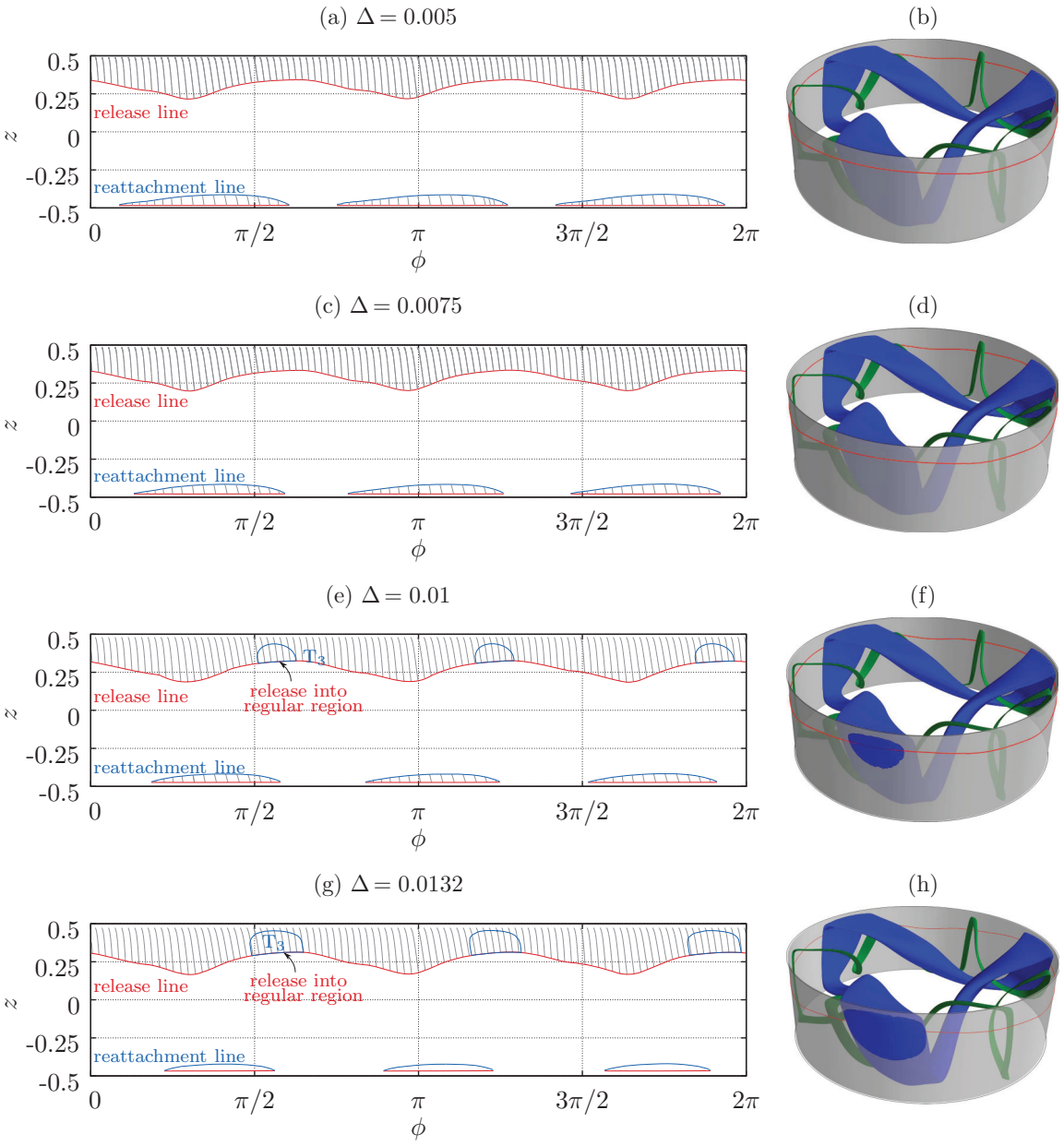

FIG. 13. (Color online) Left side: Distribution of release (red) and reattachment lines (blue) on R^* for Re = 1800 and $\Delta = 0.005$, 0.0075, 0.01, 0.0132, 0.015, 0.02, 0.0212, and 0.25, respectively. The dense nearly vertical gray lines represent the mapping of streamlines along R^*. Right side: Three-dimensional view of the KAM tori T_3^3 [blue (dark)] and T_3^6 [green (medium gray)] for the same interaction parameters, including the upper release line (red) and the surface $r = R^*$ (light gray). Note that only for $\Delta = 0.01$ (f) and larger T_3^3 periodically intersects R^* as indicated.

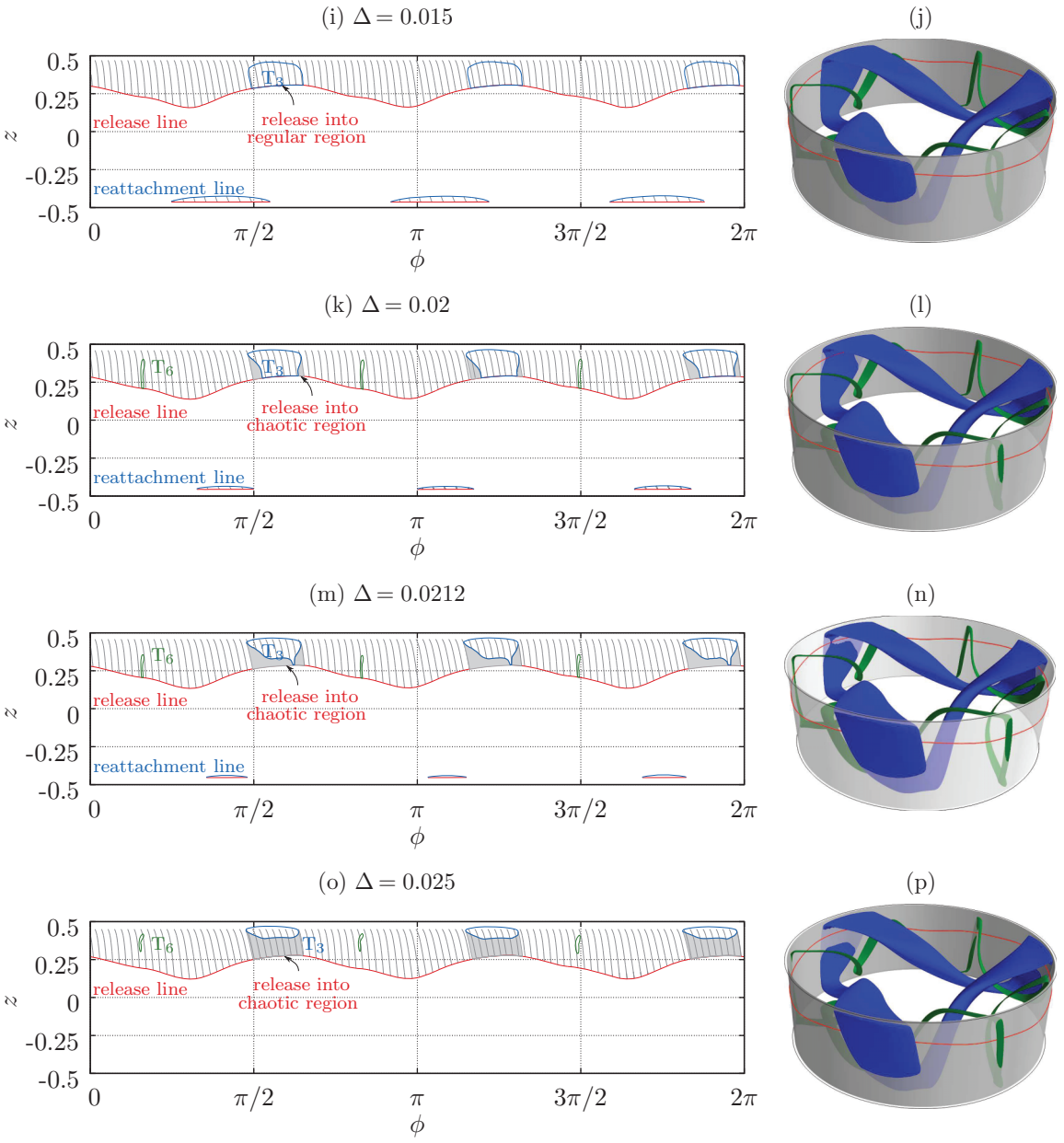

FIG. 13. (Color online) (*Continued.*)

are very weakly chaotic, because they are located in the very vicinity of the regular region.

This behavior is confirmed by Poincaré sections on the midplane $z = 0$ of 1000 streamlines released from the release line. For practical reasons these streamlines are initiated along a small circle in the midplane $z = 0$ near the axis. The first returns to the Poincaré plane are shown in Figs. 14(a) and 14(b) in which the number consecutive returns is color coded. Figures 15(a) and 15(b) show only the 20th return of each of the 1000 streamlines, hence, a total of 1000 Poincaré points. For $\Delta = 0.005$ the Poincaré points are quite scattered. For $\Delta = 0.0075$, however, the Poincaré points accumulate in the weakly chaotic region surrounding the regular region of T_3^3, without entering it. This type of accumulation has been called strange T_3^3 PAS by Muldoon and Kuhlmann [14], because all streamlines intersecting the hard wall at $r = R^*$ are mapped to a specific subset of streamlines which they called *release surface*. For $\Delta = 0.005$ and $\Delta = 0.0075$ all chaotic streamlines will ultimately be mapped to this subset which is embedded in the chaotic sea for these values of Δ. The dynamics of model particles on the subset of streamlines given by the release surface can lead to a clustering of particles on a chaotic attractor in the vicinity of the regular regions [14].

This type of less-ordered accumulation can also be seen in Figs. 16(a) and 16(b). A fuzzy accumulation structure with period three is visible in Fig. 16(b) for $\Delta = 0.0075$. The zones with enhanced particle density (red) of such strange PAS would be very difficult to detect in experiments, because a large number of particles exists (which are not shown here) which do not suffer mapping, e.g., the particles in the toroidal core.

Common to all interaction lengths considered, particles are depleted from the central region of the liquid bridge. The

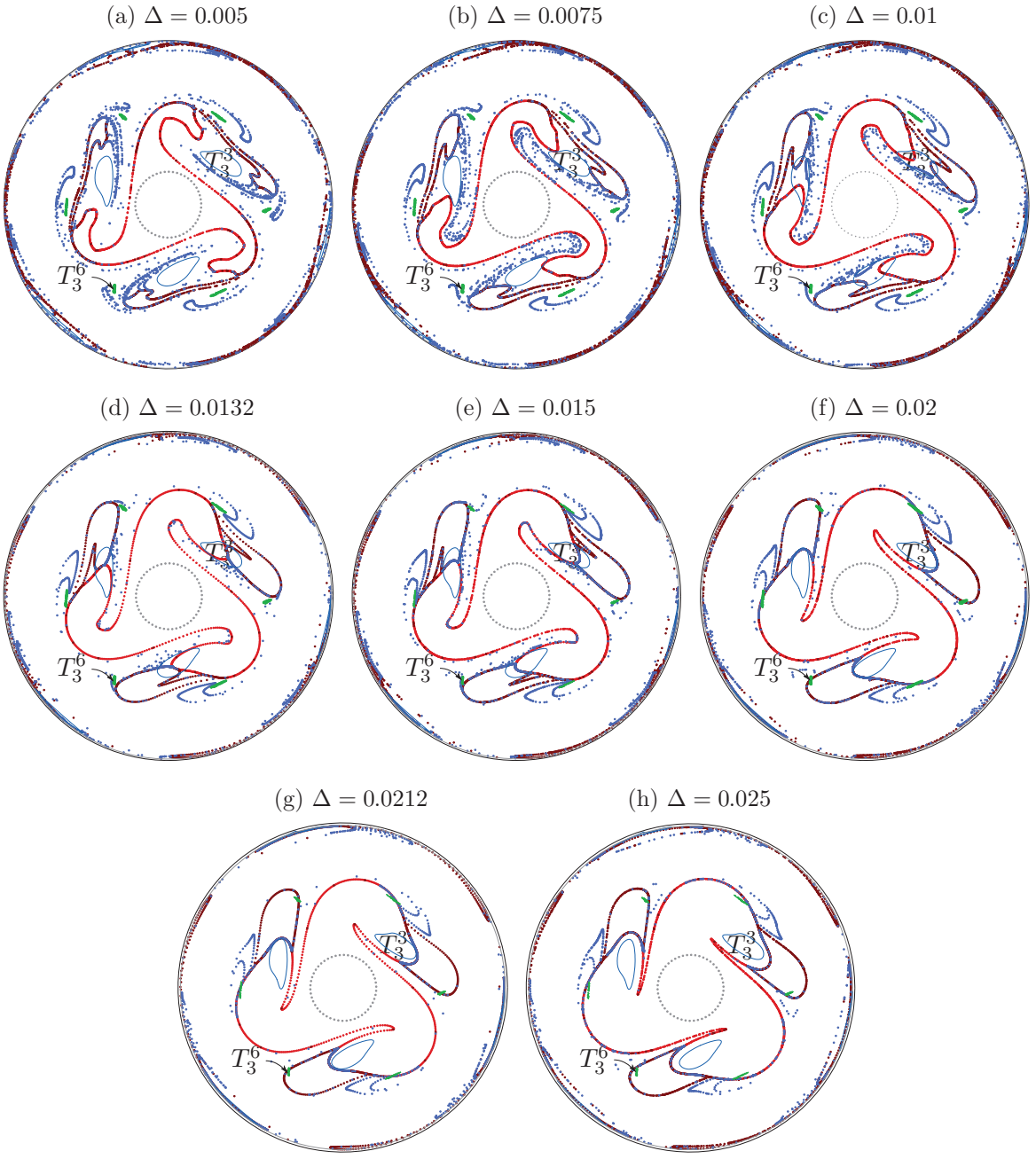

FIG. 14. (Color online) Poincaré map of 1000 streamlines showing the 1st return (red), the 2nd return (blue) and the 5th return (brown) to $z = 0$ for selected parameters Δ. The dot size is not to scale. The streamlines originate from the gray points on the near-axis circle (only every 20th initial condition is shown). The bright blue and green contours indicate the separating KAM tori for T_3^3 and T_3^6, respectively.

characteristic triangular shape would appear even sharper in Fig. 16 if the number of particles were larger. However, in all Poincaré sections of Figs. 14 and 15 for particles released from the release line, an area near the axis, which resembles a triangle with curved corners, remains free of Poincaré points. This happens because this region is unaccessible for mapped streamlines (particles having interacted with the free surface). Therefore, particles can leave this region, but they cannot enter it.

b. $\Delta = 0.01$: *Tubular PAS*. For $\Delta = 0.01$ the T_3^3-KAM system of tubes intersects R^* [Figs. 13(e) and 13(f)]. The blue line in Fig. 13(e) indicates the part of the contour of the separating KAM torus of T_3^3 above the release line. Regular as well as chaotic streamlines from above the release line are mapped along the gray lines and part of them are released to the regular region of T_3^3. This means that particles from the chaotic sea are transferred into the regular region of T_3^3 where they can possibly accumulate. From the Poincaré sections [Figs. 14(c) and 15(c)] one can observe that the streamlines are mapped to the regular region and form a tubular structure inside the regular T_3^3 region after the first few returns to $z = 0$. The accumulation structure resulting from irregularly distributed

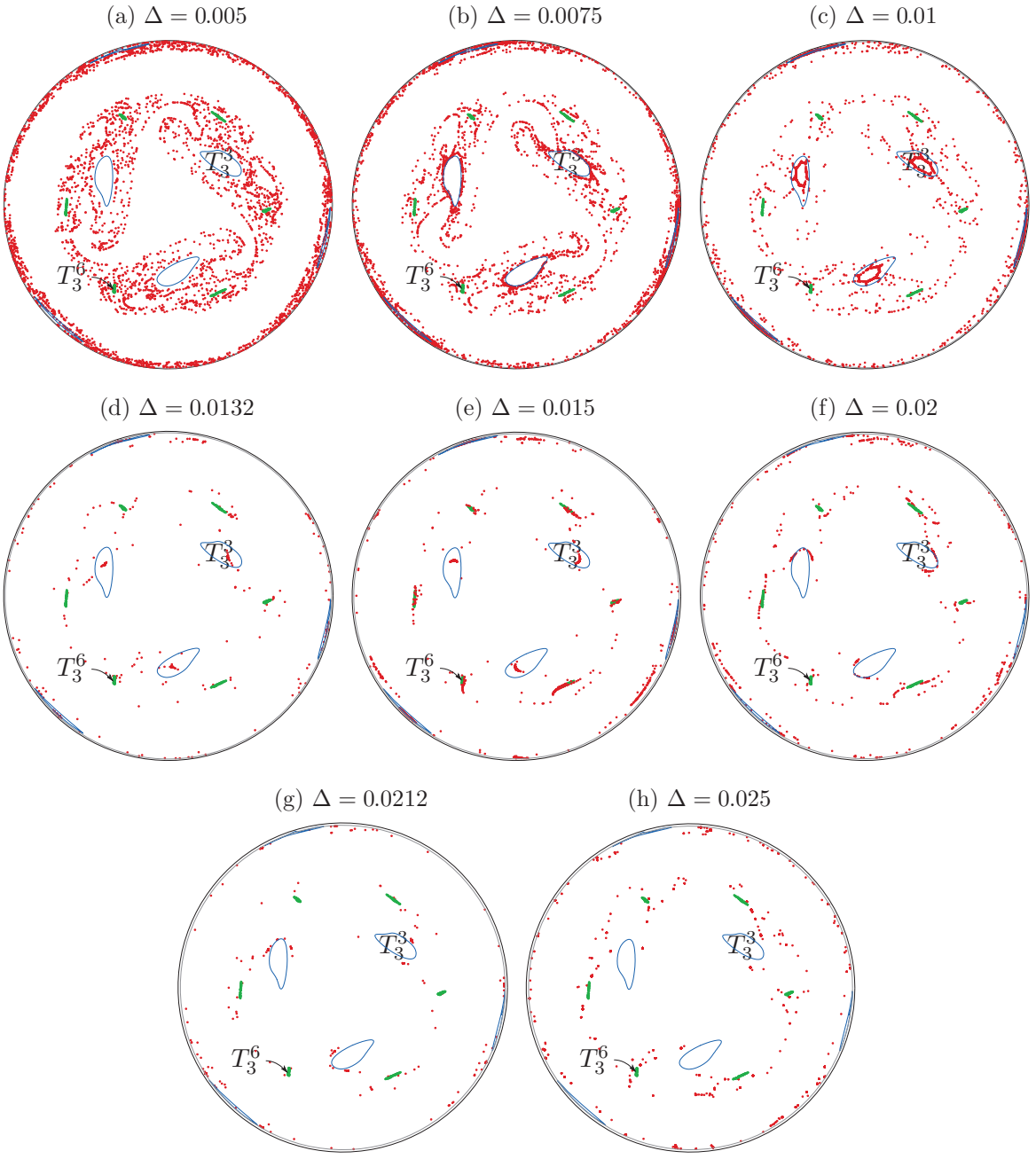

FIG. 15. (Color online) Poincaré map of the 20th returns to the Poincaré plane $z = 0$ of 1000 streamlines (red dots, not to scale) for selected parameters Δ. The blue contour indicates T_3^3 and the green dots indicate T_3^6.

initial conditions is clearly seen in Fig. 16(c). In an axial view this tubular PAS of T_3^3 type appears relatively broad with enhanced edges.

c. $\Delta = 0.0132$: *Linelike PAS*. As Δ is increased, the tubular T_3^3 PAS created by the mapped streamlines becomes more slender and reduces to a closed PAS line when the closed streamline L_3^3 becomes tangent to R^* [13,14]. For the T_3^3 system this happens at $\Delta = \Delta_L = 0.01325$. Linelike PAS for $\Delta = \Delta_L$ is identical with the central closed streamline of the KAM system. In this case all streamlines of the KAM system experience a mapping. We find that after a few mappings a large number of streamlines have been mapped exactly to the central closed streamline L_3^3 [Fig. 15(d)], as predicted. This becomes even clearer in the accumulation pattern shown in Fig. 16(d). Perfect and sharp linelike PAS is formed.

d. $\Delta = 0.015$ and $\Delta = 0.02$: *Period-doubled PAS*. For $\Delta = 0.015 > \Delta_L$ the three wings of the depletion triangle reach far into the regular regions and have even crossed L_3^3 [Fig. 14(e)]. In the top view shown in Fig. 16(e) the accumulation structure is relatively sharp and exhibits the well-known $m = 3$ PAS. Closer inspection shows, however, that the PAS is not perfectly linelike. The accumulation structure inside T_3^3 seems to be ribbonlike [Fig. 15(e)] and in the axial projection in Fig. 16(e) PAS seems to consist of two nearby linelike structures.

In addition to T_3^3-PAS the separating T_3^6 KAM torus almost touches $r = R^*$. Therefore, strange PAS of type T_3^6 is expected.

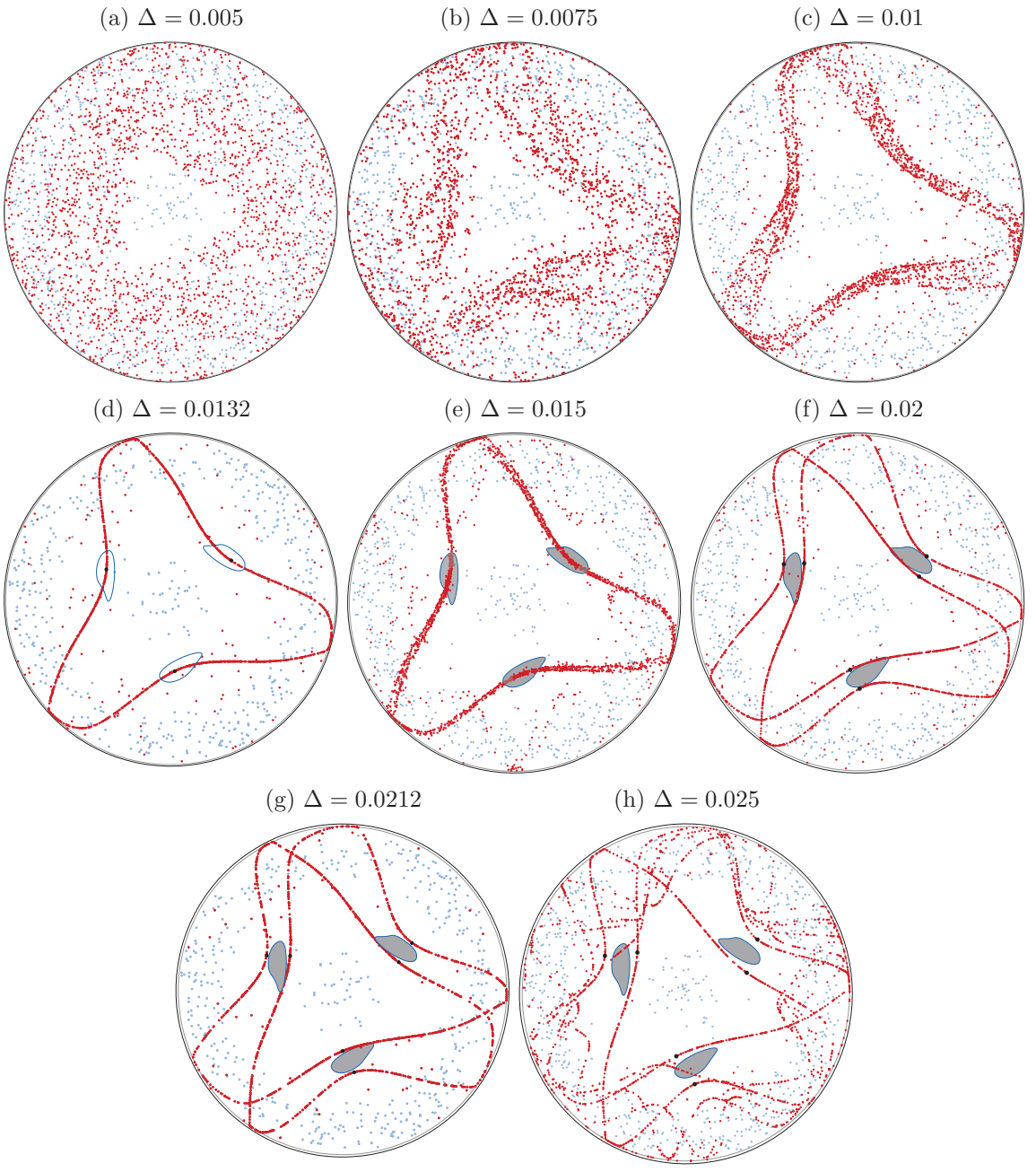

FIG. 16. (Color online) Axial view on the distribution of 5000 fluid particles at $t = 5$ after they were initiated at random locations. Red (dark) dots indicate particles that have been mapped at least once, and blue (gray) dots those that have never been mapped. The six black points in (f), (g), and (h) represent the intersection points of the doubly periodic T_3^3 PAS with the plane $z = 0$. These points lie outside of the contour of the separating T_3^3 KAM torus in that plane (gray areas, blue contour), hence, in the chaotic sea.

In Fig. 15(e) many streamlines (red) have been mapped to the close vicinity of the tiny separating T_3^6 KAM tube, shown in green. Also Fig. 16(e) shows, besides T_3^3 PAS, a weak indication of the T_3^6 structure.

A further increase of the interaction length to $\Delta = 0.02$ leads to a situation close to pinching for T_3^3 [Figs. 13(k) and 13(l)]. In this case, a significant number of streamlines from the regular region are mapped to a chaotic state. The depletion triangle in the midplane covers almost the entire regular region of T_3^3 [Fig. 14(f)].

After 20 returns to the Poincaré plane almost all streamlines have been attracted to a limit cycle. The limit cycle is closed only after two full revolutions about the axis. Since the structure repeats itself after two returns to the free surface, this PAS represents a period-doubled or a subharmonic T_3^3-type of PAS. The limit cycle is located in the chaotic region, but near the regular T_3^3 region [Figs. 15(f) and 16(f)]. It consists of two different segments of chaotic streamlines with short segments on R^* which have an azimuthal period of $4\pi/3$. The stabilization of a chaotic streamline by the dissipation associated

with the free-surface interaction seems to be similar to the one found by Kuhlmann and Muldoon [58] for a model flow.

For $\Delta = 0.02$ also T_3^6 intersects R^* [Figs. 13(k) and 13(l)]. However, the segment of the release line inside of the separating T_3^6 KAM tube is very small. Therefore, only a small fraction of the streamlines are mapped to the regular region of T_3^6. One can see, however, that the release surface (the border of the depletion zone) intersects the tiny contour of the regular T_3^6 region in Fig. 14(f) right in the middle. Due to the small efficiency to attract particles, T_3^6 PAS is not seen in Fig. 16(f). If many more particles would have been used, linelike T_3^6 PAS were visible for $\Delta = 0.02$.

e. $\Delta = 0.0212$. At the pinch point $\Delta = \Delta_p = 0.0212$, which is clearly visible in Figs. 13(m) and 13(n), we find a similar behavior as for $\Delta = 0.02$. The period-doubled PAS has moved further into the chaotic range of streamlines [Fig. 15(g)] and the period doubling is even more pronounced [Fig. 16(g)].

f. $\Delta = 0.025$, For $\Delta = 0.025$ [Figs. 13(o) and 13(p)], beyond the pinching of both T_3^3 and of T_3^6, all streamlines, including those of the regular region, are mapped into the chaotic state. Nevertheless, we find accumulation structures in the chaotic region which are far away from both regular regions. The accumulation pattern in Fig. 16(h) is linelike and seems to be composed of a superposition of period-doubled T_3^3 PAS and linelike structures resembling T_3^6 PAS.

V. DISCUSSION

A. Particle-depletion zone and the core of particles

Two phenomena related to PAS can be reliably reproduced in experiments with nearly density-matched particles. One phenomenon is a rotating polygonal depletion zone in traveling hydrothermal waves with azimuthal wave number $m \geqslant 2$. The depletion zone is very robust and it exists at relatively low, slightly supercritical Reynolds numbers for which linelike PAS is not observed [9,50,52,59,60]. The other phenomenon, existing at higher Reynolds numbers, is a thick ring of particles near the circle which would mark the center of the steady axisymmetric basic vortex. Linelike PAS is found to wind around this ring of particles which has been called *toroidal core of particles* [9] (see Fig. 17). When PAS and the core of particles arise, the polygonal depletion zone is no longer visible.

The polygonal depletion zone, which can also be be seen in Fig. 16, has been explained for a model flow by Muldoon and Kuhlmann [14]. It is due to the mapping of streamlines to the release line. The release line is closed and makes one full azimuthal revolution about the liquid bridge. Therefore, it defines a particular stream tube which rolls up internally. The stream tube can develop a very complex structure downstream due to repeated mappings [14]. This stream tube, also called release surface, is significant in the framework of the hard-wall model, because all particles which are mapped to the release line are restricted to move on the release surface, which is a certain subset of all streamlines for all times. All Poincaré points shown in Figs. 14 and 15 lie on the release surface. In particular, the Poincaré points of the first return to $z = 0$ in Fig. 14 represents the envelope of the release surface. Due to the mapping on R^* particles cannot reach streamlines which intersect R^* below the release line. Those streamlines intersect $z = 0$ inside of the depletion triangle. Therefore, particles are removed from this region. The depletion zone is created immediately, essentially after a single revolution of the basic vortex. For small Reynolds numbers such that $\Delta_m > \Delta$ for all KAM tubes, KAM tubes do not intersect $r = R^*$ and only chaotic streamlines are mapped. Therefore, mapped particles remain suspended in the chaotic sea but are restricted to the release surface. In this case, the depletion zone becomes clearly visible as a hallmark of the streamline mapping. The existence of the depletion zone in experiments as well as in the hard-wall model is a strong indicator for the validity of the hard-wall model.

At higher Reynolds numbers with $\Delta_m < \Delta$ a tubular or linelike PAS is created. In this case all particles are typically removed from the chaotic sea and transferred to the PAS by the mapping of streamlines and the mechanism explained by Hofmann and Kuhlmann [13]. For that reason, the depletion zone no longer can be recognized. However, density-matched particles remain suspended inside of those regular tori which do not intersect with R^*. This is typically the case for the toroidal core T_{core}. The core of particles observed by Tanaka *et al.* [9] thus can be explained by particles suspended in the KAM torus T_{core}.

Contrary to the Tanaka *et al.* [9] experiments for $\text{Pr} = 28$, neither the depletion zone nor the core of particles has been reported by Schwabe *et al.* [11] for $\text{Pr} = 8$. In both cases the flow is nearly incompressible. Therefore, density-matched particles should remain suspended in the chaotic domain outside of the depletion zone in the absence of PAS and also in the core T_{core}. For non-density-matched particles these phenomena should be transient. Since Tanaka *et al.* [9] observed both phenomena, even for particles which are

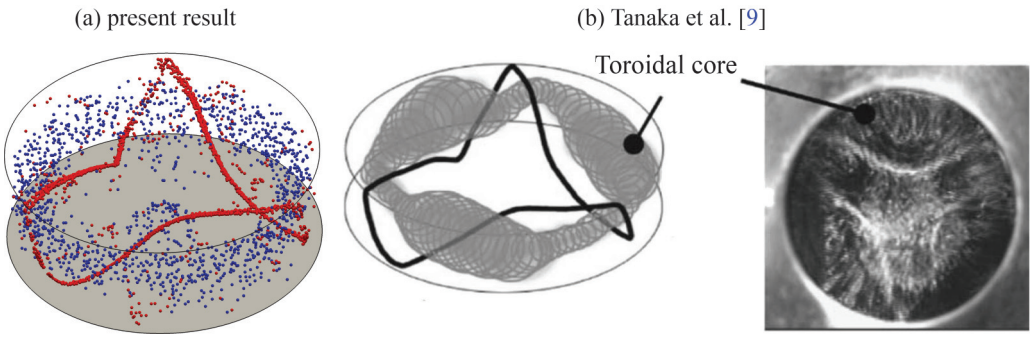

FIG. 17. (Color online) Visual comparison of (a) calculated PAS for $\text{Pr} = 4$, $\text{Re} = 1800$, and $\Delta = 0.015$ and (b) experimental observation of PAS for $\text{Pr} = 28$ (Fig. 11 of Ref. [9]).

significantly heavier than the liquid, any forces on the small particles in the bulk must be very weak. This is consistent with our model assumptions. The polygonal depletion zone and the core have also been observed by Schwabe [54], but they were not mentioned in Ref. [11], because these authors did not focus on the transient phenomena and considered the asymptotic state for long times (after hours).

Derived from these considerations, all numerical simulations of the particle motion using density-matched particles or particles with a small Stokes number must reproduce the depletion zone and the core of particles for an unlimited time or for a relatively long period of time, respectively, which is dictated by the Stokes number. If the depletion zone for sufficiently small Reynolds numbers vanishes due to loss of particles from the chaotic sea or if particles are lost prematurely from the core this behavior is a signal of additional dissipation in the code which may fake particle-accumulation patterns which are not solutions of the governing differential equations, hence, nonphysical.

B. PAS formation time

The PAS formation time is of interest [11,21], in particular, for linelike PAS, because it is usually very short and because the formation time can allow a distinction between different mechanisms of PAS formation, e.g., the particle–free-surface interaction, pressure-gradient forces, or numerical error accumulation. Several processes either contribute to or counteract linelike PAS formation. (a) Hofmann and Kuhlmann [13] described the process by which particles are mapped exclusively inside the regular region to form PAS. The rate of this process depends on the volume flux through R^* within the area limited by the contour of the separating KAM torus on R^* for which intersecting streamlines are mapped to the segment of the release line inside the KAM set (region 0 and 1 in Fig. 12). Also the winding angle about the central closed streamline plays a role [13]. (b) In addition, the volume flux through R^* in region 4 contributes to PAS formation. This volume flux can be a substantial contribution to PAS by transferring particles from chaotic streamlines to regular ones. Assuming that any chaotic streamline, after a sufficiently long evolution time, will intersect R^* in region 4, this process may lead to a complete drainage of particles from the chaotic sea to the regular region and, thus, to PAS. This effect explains the complete depletion of major regions of the liquid bridge, except from those regular regions which do not intersect R^*, e.g., the core T_{core}. (c) The third process which determines the formation time of linelike PAS is the loss of particles from the regular region by streamline mapping from regular to chaotic streamlines which occurs in regions 2 and 3 in Fig. 12. Close to pinching, this latter process counteracts PAS formation inside the regular region by removing particles from the regular region, while the redistribution of particles within the regular region (regions 0 and 1 in Fig. 12) becomes less important. We have seen, however, that the linelike PAS can move out of the regular region and into the chaotic sea.

Due to these different particle-redistribution processes the formation time for PAS cannot easily be estimated and it must be obtained by numerical simulation of a sufficient number of particle trajectories (see, e.g., Refs. [14,21]).

C. Injection point

The collection of particles near the free surface has already been mentioned by Tanaka *et al*. [9] and Schwabe *et al*. [10], who speak of *injection* (of particles into the bulk of the liquid) when describing their experimental observations. Schwabe *et al*. [11] write about a particular *injection point* and Schwabe and Mizev [57] mention *gathering and injection*. We confirm these observations and suggest a surface mechanism which leads to the gathering of particles: the transfer of particles from the chaotic sea to the regular KAM tori and also the subsequent focusing of the particles by a transfer among regular (as well as chaotic) streamlines as described by Hofmann and Kuhlmann [13].

D. Comparison with Hofmann and Kuhlmann [13]

Hofmann and Kuhlmann [13] considered finite-size tracers using the same particle–free-surface interaction model. They investigated only one particle size corresponding to $\Delta = 0.015$. On a relatively coarse mesh they found linelike PAS of type T_3^3. The slight splitting of the PAS for $\Delta = 0.015$ was not noticed, probably because of the coarse resolution of the flow field. They found the winding angle $\theta \approx \pi$ of regular streamlines about L_3^3 between two successive mappings. Within the iterated map for the release point suggested by Hofmann and Kuhlmann [13] $\theta = \pi$ means a periodic oscillation of the release point. Therefore, the convergence to linelike PAS by a mapping exclusively among regular streamlines is significantly slowed down for $\theta \to \pi$. Nevertheless, the mapping of chaotic streamlines into the regular region provides a rapid process. Hence, PAS for $\Delta = 0.015$ seems to form on two different time scales: rapid mapping of chaotic streamlines to the regular region and a slow focusing onto linelike PAS inside of the regular region.

E. Period doubling of linelike PAS

A new feature of PAS found is the period doubling of T_3^3 PAS for interaction parameters beyond the pinch point $\Delta > \Delta_p$. Period-doubled PAS previously has been found by Domesi [61] for $\Delta = 0.03$, using a variant of the Maxey-Riley equation to describe the motion of heavy particles with $\rho_p/\rho_f = 4$. The period doubling of linelike PAS can be noticed for $\Delta = 0.015$ which is slightly larger than Δ_p.

Period doubling is not present in the simple iterative map of Ref. [13] for the release point of linelike PAS. Their model assumes KAM tubes of circular cross section. One difference between the iterative map of Ref. [13] and the mapping based on the Navier-Stokes flow is the asymmetry of the cross section of the KAM tubes. In Appendix we show that an asymmetrically extended iterative map also shows period doubling. Hence, the period doubling is likely to be associated with the asymmetry of the KAM tubes.

F. Increasing Reynolds numbers

For the PAS which are located in the regular regions of the flow the efficiency of PAS formation is related to the length of the release-line segments inside the separating KAM torus. Because the separating KAM tori become thinner the higher the Reynolds number, it is likely that the PAS formation time

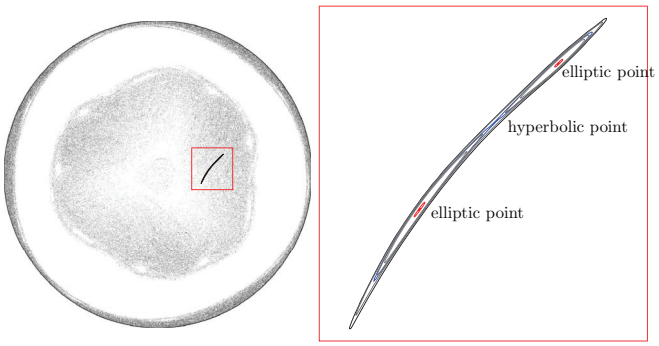

FIG. 18. (Color online) (a) Poincaré section in the plane $z = 0$ for $\mathrm{Re} = 3000$. The square box indicates the zoom into the system of KAM tori of type T_3^3 shown in (b). Note the hyperbolic point between two elliptic points.

will, in general, increase for increasing Reynolds numbers. As an example, Fig. 18(a) shows a Poincaré plot at $z = 0$ for $\mathrm{Re} = 3000$ in which the separating KAM torus T_3^3 is outlined by a thin closed black line. A zoom into the T_3^3 region, indicated by the rectangle, is shown in Fig. 18(b). It can be seen that the separating KAM torus is extremely squeezed and that it accommodates, apart from two elliptic fixed points, a hyperbolic fixed point in its center. By increasing the Reynolds number to $\mathrm{Re} = 3000$ the central elliptic closed streamline L_3^3 has become unstable and turned into a hyperbolic closed streamline. The two new elliptic points have been created by a period-doubling bifurcation. In the Poincaré map, both elliptic points are visited alternatingly. Since the Feigenbaum scenario is one possible route by which KAM tori vanish upon parameter variation [62], we speculate that T_3^3 will vanish completely for slightly higher Reynolds numbers. As we have seen for the period-doubled PAS, however, PAS can also form in the weakly chaotic region (see also Ref. [58]). Therefore, it is difficult to predict an upper bound on Re for which PAS will cease to exist for any interaction length Δ.

In any case, the range of interaction lengths for which linelike PAS exists is expected to shrink with increasing Reynolds number, because the KAM tori become thinner. Since the interaction length is expected to be strongly correlated with the particle size, this would also mean that the range of particles sizes for which PAS can be expected will shrink with increasing Reynolds numbers.

Another limiting factor for the existence of PAS is the range of Reynolds numbers for which pure traveling hydrothermal waves exist. Velten *et al.* [5] have shown that the windows of the aspect ratio and the Reynolds number for the existence of pure traveling hydrothermal waves is quite restricted. This is particularly true for liquids with high Prandtl numbers for which the flow is often quasiperiodic even slightly above the critical threshold Reynolds number. It is expected that PAS are suppressed by any incommensurate frequency because no steady streamlines exist for a quasiperiodic flow in any frame of reference.

VI. CONCLUSIONS

We have carried out high-fidelity numerical Navier-Stokes calculations for hydrothermal waves in liquid bridges. For $\mathrm{Pr} = 4$ and $\Gamma = 0.66$ we found that regular and chaotic motion coexist for $\mathrm{Re} = 1800$, 2600, and 3000. Due to the high resolution we unambiguously identified various sets of KAM tori in the rotating frame of reference. This enabled a reliable computation of streamlines for a long period of time, minimizing the flow-field interpolation error.

Experimental results indicate that a strong dissipation exists for the motion of suspended particles which is located in a thin subsurface layer of the free surface, while dissipation is negligible in the bulk. The simplest dissipation model taking these conditions into account is an inelastic hard-wall particle–free-surface interaction model. The only parameter in this model is the thickness of the dissipation zone, which we call the interaction length Δ. The hard-wall model implies a mapping among streamlines on which particles move, equivalent to a particle transfer from one streamline to another. The streamline mapping leads to particle accumulation structures which depend on the interaction length. The types of PAS found (strange, tubular, or linelike) using the hard-wall model are consistent with the results of Hofmann and Kuhlmann [13] for the Navier-Stokes flow and qualitatively similar to the results of Muldoon and Kuhlmann [14] for a model flow. However, the present results are much more accurate than the previous numerical data based on the Navier-Stokes equations which were not able to sufficiently resolve the velocity field. The hard-wall model can explain the rotating particle depletion zones which are robust features of experimental hydrothermal waves. Linelike PAS is predicted for a certain range of interaction lengths which should strongly correlate with the particle size. For all interaction lengths considered the hard-wall model preserves a toroidal core of neutrally buoyant particles, as is also observed in experiments, even for non-neutrally-buoyant particles. Linelike PAS and the toroidal core are shown in Fig. 17 in comparison with the experimental result of Tanaka *et al.* [9]. Despite the different Prandtl numbers, the agreement is remarkable. We conclude that the hard-wall model for the motion of suspended particles captures the essential mechanism leading to PAS.

It may be noted that the linelike particle accumulation in our model is due to a structural instability of elliptic orbits (see, e.g., Ref. [63]). PAS is thus understood as the creation of attractors by dissipative perturbations of a volume preserving three-dimensional steady flow. Kuhlmann and Muldoon [21] have shown for a model problem that the limit cycles (linelike PAS) grow out of the elliptic orbits (central closed streamlines of the KAM tori) as the dissipation is continuously increased by, e.g., pressure-gradient forces and the Stokes drag, which could be treated as a small perturbation. In the case of the inelastic hard-wall model the dissipative perturbations for a given interaction length Δ is of $O(1)$. This leads to an $O(1)$ effect immediately, e.g., the polygonal depletion zone. Thus the mechanism of PAS is as simple as the dynamics of a dissipative system under a three-dimensional steady flux. The action of the dissipative mechanism proposed here is, however, not trivial, because the streamline mapping leads to a discontinuous dynamical model (hybrid dynamical system).

As a qualitatively new feature we predict period-doubled PAS for $\mathrm{Pr} = 4$. It would be of great interest to proof or disproof this prediction by corresponding experiments. Future numerical investigations should consider the flow for higher

Prandtl numbers for which most experiments have been carried out. This would enable to further explore the potential and the limitations of the hard-wall model. Such flow simulations may be even more demanding computationally, as the thermal boundary layers become thinner the higher the Prandtl number. Another challenge is the improvement of the particle–free-surface interaction model. This would require, however, a detailed two-way coupled study of the particle motion near the thermocapillary free surface.

ACKNOWLEDGMENTS

The authors gratefully acknowledge support from ESA under Contract No. 4000103003 and from ZID of Vienna University of Technology by providing computing time on the Vienna Scientific Cluster. We thank Ernst Hofmann and Dietrich Schwabe for many stimulating discussions.

APPENDIX: EXTENSION OF THE MODEL OF HOFMANN AND KUHLMANN [13]

Extending the iterated map of Hofmann and Kuhlmann [13], we demonstrate that the period doubling can be caused by an asymmetry of the KAM torus. This asymmetry is due to the broken mirror symmetry ($\varphi \to -\varphi$) of the hydrothermal wave and can be clearly seen for the torus T_3^3 in Fig. 8. To that end we consider the iterated map [13] for the release point (x_n, y_n) of particles in the regular region,

$$x_{n+1} = x_n \cos\theta_n - y_n \sin\theta_n, \tag{A1a}$$

$$y_{n+1} = \min\left[A, x_n \sin\theta_n + y_n \cos\theta_n\right], \tag{A1b}$$

where (x, y) corresponds to local azimuthal and radial coordinates centered at the closed streamline (for the details, see Ref. [13]). The index n numbers the returns to the free surface for a particular initial condition and θ_n is the winding angle. For $\Delta \geqslant \Delta_L$ the parameter $A \simeq \Delta_L - \Delta < 0$ is negative. Since A is the only length scale in the map (A1) we can set $A = -1$ without loss of generality. The model (A1) is based on the assumption that the KAM tubes have concentric circular cross sections. For a constant winding angle $\theta_n = \text{const}$ period-doubled limit cycles are absent [13].

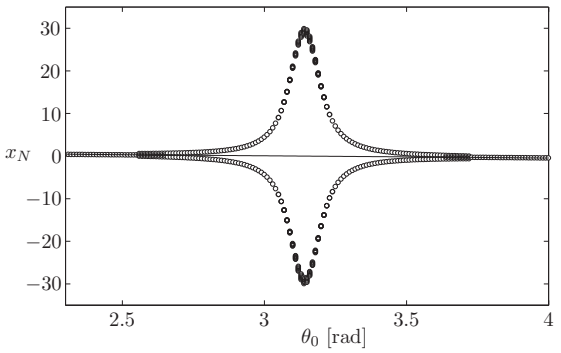

FIG. 19. Fixed points of the map (A1) as function of θ_0 for $\Delta\theta = 0.1$. The fixed point $x = \tan^{-1}(\theta_0/2)$ for $\Delta\theta = 0$ [13] is shown as a full line. For each θ_0 the values x_N for $N = 1000$ are plotted for 11 initial conditions.

To mimic the asymmetry of the KAM tubes we assume that the winding angle θ between successive returns to the free surface depends on x_n,

$$\theta_n = \theta_0 \pm \frac{\Delta\theta}{2}, \quad \text{if} \quad x_n \gtrless 0. \tag{A2}$$

The attracting limit cycle is shown in Fig. 19 by plotting the release point of the limit cycle $\lim_{n\to\infty} x_n \approx x_N$ (N large) as function of the mean winding angle θ_0 using 11 representative initial conditions conditions on R^* corresponding to $y_0 = -1$ and $x_0 = [-5, -4, \ldots, 5]$. The full line indicates the release point for the simply periodic limit cycle for $\theta_n = \theta_0$. With $\Delta\theta = 0.1$, however, we find period doubling near $\theta_0 = \pi$, which is indicated by the two release points which are visited alternatingly. The convergence to the period-2 orbit is still slow for $\theta_0 \approx \pi$, as can be seen from the slight scatter of the 11 data points.

For given θ_0 and $\Delta\theta$ the separation between the two Poincaré points x_n of the period-doubled solution scales with the distance $|A|$ of the closed streamline L_i^j from $r = R^*$. For $\theta_0 = \pi$, a condition which is approximately satisfied for the Navier–Stokes flow and T_3^3 [13], the period-doubling bifurcation occurs at $\Delta = \Delta_L$. This explains the minute period doubling seen in Fig. 16(d) for Δ slightly larger than Δ_L.

[1] *Handbook of Crystal Growth*, edited by D. T. J. Hurle (North-Holland, Amsterdam, 1994).
[2] T. DebRoy and S. A. David, Rev. Mod. Phys. **67**, 85 (1995).
[3] A. Cröll, W. Müller-Sebert, K. W. Benz, and R. Nitsche, Micrograv. Sci. Technol. **3**, 204 (1991).
[4] F. Preisser, D. Schwabe, and A. Scharmann, J. Fluid Mech. **126**, 545 (2006).
[5] R. Velten, D. Schwabe, and A. Scharmann, Phys. Fluids A **3**, 267 (1991).
[6] H. C. Kuhlmann, *Thermocapillary Convection in Models of Crystal Growth*, Vol. 152 of Springer Tracts in Modern Physics (Springer, Berlin, 1999).
[7] H. Kawamura and I. Ueno, in *Surface Tension-Driven Flows and Applications*, edited by R. Savino (Research Signpost, Trivandrum, Kerala, 2006), Chap. 1, pp. 1–24.
[8] D. Schwabe, P. Hintz, and S. Frank, Micrograv. Sci. Technol. **9**, 163 (1996).
[9] S. Tanaka, H. Kawamura, I. Ueno, and D. Schwabe, Phys. Fluids **18**, 067103 (2006).
[10] D. Schwabe, S. Tanaka, A. Mizev, and H. Kawamura, Micrograv. Sci. Technol. **18**, 117 (2006).
[11] D. Schwabe, A. I. Mizev, M. Udhayasankar, and S. Tanaka, Phys. Fluids **19**, 072102 (2007).
[12] Yukiko Abe, Ichiro Ueno, and Hiroshi Kawamura, Ann. N. Y. Acad. Sci. **1161**, 240 (2009).
[13] Ernst Hofmann and Hendrik C. Kuhlmann, Phys. Fluids **23**, 0721106 (2011).
[14] F. H. Muldoon and H. C. Kuhlmann, Physica D **253**, 40 (2013).
[15] D. O. Pushkin, D. E. Melnikov, and V. M. Shevtsova, Phys. Rev. Lett. **106**, 234501 (2011).

[16] Hendrik C. Kuhlmann and Frank H. Muldoon, Phys. Rev. Lett. **108**, 249401 (2012).
[17] D. O. Pushkin, D. E. Melnikov, and V. M. Shevtsova, Phys. Rev. Lett. **108**, 249402 (2012).
[18] M. R. Maxey and J. J. Riley, Phys. Fluids **26**, 883 (1983).
[19] George Haller and Themistoklis Sapsis, Physica D **237**, 573 (2008).
[20] T. Sapsis and G. Haller, Chaos **20**, 017515 (2010).
[21] H. C. Kuhlmann and F. H. Muldoon, Phys. Rev. E **85**, 046310 (2012).
[22] F. H. Muldoon and H. C. Kuhlmann, Comput. Fluids **88**, 43 (2013).
[23] J. M. Ottino, *The Kinematics of Mixing: Stretching, Chaos, and Transport*, Cambridge Texts in Applied Mathematics (Cambridge University Press, Cambridge, 1989).
[24] H. Aref, J. Fluid Mech. **143**, 1 (1984).
[25] H. Aref and S. Balachandar, Phys. Fluids **29**, 3515 (1986).
[26] W.-L. Chien, H. Rising, and J. M. Ottino, J. Fluid Mech. **170**, 355 (2006).
[27] D. Kroujiline and H. A. Stone, Physica D **130**, 105 (1999).
[28] K. Bajer, Chaos Solitons Fractals **4**, 895 (1994).
[29] Y. Mizuno and M. Funakoshi, Fluid Dynam. Res. **35**, 205 (2004).
[30] H. A. Kusch and J. M. Ottino, J. Fluid Mech. **236**, 319 (2006).
[31] G. O. Fountain, D. V. Khakhar, I. Mezić, and J. M. Ottino, J. Fluid Mech. **417**, 265 (2000).
[32] M. K. Smith and S. H. Davis, J. Fluid Mech. **132**, 119 (2006).
[33] M. Wanschura, V. S. Shevtsova, H. C. Kuhlmann, and H. J. Rath, Phys. Fluids **7**, 912 (1995).
[34] J. Leypoldt, H. C. Kuhlmann, and H. J. Rath, J. Fluid Mech. **414**, 285 (2000).
[35] J. Leypoldt, H. C. Kuhlmann, and H. J. Rath, Adv. Space Res. **29**, 645 (2002).
[36] J. Plateau, *Statique expérimentale et théorique des liquides soumies aux seules forces molécularies* (Gauthier-Villars, Paris, 1873).
[37] G. Mason, J. Colloid. Interface Sci. **32**, 172 (1970).
[38] R. Finn and T. I. Vogel, Z. Anal. Anwendungen **11**, 3 (1992).
[39] S. Albensoeder and H. C. Kuhlmann, J. Comput. Phys. **206**, 536 (2005).
[40] OPENFOAM *User Guide* (2012), http://www.openfoam.org.
[41] S. J. Cowley and S. H. Davis, J. Fluid Mech. **135**, 175 (2006).
[42] D. Canright, Phys. Fluids **6**, 1415 (1994).
[43] A. Zebib, G. M. Homsy, and E. Meiburg, Phys. Fluids **28**, 3467 (1985).
[44] *VTK Toolkit Documentation*, http://www.vtk.org/VTK/help/documentation.html.
[45] Ch. Nienhüser, Ph.D. thesis, University of Bremen, 2002.
[46] M. K. Smith, Phys. Fluids **29**, 3182 (1986).
[47] D. Melnikov, D. Pushkin, and V. Shevtsova, Eur. Phys. J. Special Top. **192**, 29 (2011).
[48] I. Ueno *et al*. (private communication, 2013).
[49] H. C. Kuhlmann, R. V. Mukin, T. Sano, and I. Ueno (unpublished).
[50] I. Ueno, Y. Ono, D. Nagano, S. Tanaka, and H. Kawamura, in *4th JSME–KSME Thermal Engineering Conference*, *Kobe, Japan, October, 2000* (Japanese Society of Mechanical Engineers), Vol. III, pp. 265–270.
[51] H. Kawamura, I. Ueno, and T. Ishikawa, Adv. Space Res. **29**, 611 (2002).
[52] I. Ueno, S. Tanaka, and H. Kawamura, Phys. Fluids **15**, 408 (2003).
[53] I. Ueno (private communication 2013).
[54] D. Schwabe (private communication 2013).
[55] S. Domesi, Microgravity Sci. Technol. **18**, 137 (2006).
[56] D. Schwabe and S. FrankAdv. Space Res. **23**, 1191 (1999).
[57] D. Schwabe and A. I. Mizev, Eur. Phys. J. Special Top. **192**, 13 (2011).
[58] H. C. Kuhlmann and F. H. Muldoon, Eur. Phys. J. Special Top. **219**, 59 (2013).
[59] K. Noguchi, I. Ueno, S. Tanaka, H. Kawamura, and K. Nishino, in *11th International Symposium on Flow Visualization*, *Notre Dame, Indiana, USA, August*, 2004 (University of Notre Dame, Optimage Ltd., Edinburgh, UK, 2004), p. 79.
[60] M. Nishimura, I. Ueno, K. Nishino, and H. Kawamura, Exp. Fluids **38**, 285 (2005).
[61] S. Domesi, Ph.D. thesis, University of Bremen, 2008.
[62] A. J. Lichtenberg and M. A. Lieberman, *Regular and Stochastic Motion*, Vol. 38 of Applied Mathematical Sciences (Springer, Berlin, 1983).
[63] J. Guckenheimer and P. Holmes, *Nonlinear Oscillations, Dynamical Systems, and Bifurcations of Vector Fields*, Vol. 42 of Applied Mathematical Sciences (Springer, Berlin, 1983).